Inorganic Chemistry
Article

Inorg. Chem. **2009**, *48*, 7905–7921 **7905**
DOI: 10.1021/ic900831q

Unsymmetrical $Fe^{III}Co^{II}$ and $Ga^{III}Co^{II}$ Complexes as Chemical Hydrolases: Biomimetic Models for Purple Acid Phosphatases (PAPs)

Fernando R. Xavier,[†] Ademir Neves,*[,†] Annelise Casellato,[†] Rosely A. Peralta,[†] Adailton J. Bortoluzzi,[†] Bruno Szpoganicz,[†] Patricia C. Severino,[‡] Hernán Terenzi,[‡] Zbigniew Tomkowicz,[§,⊥] Sergei Ostrovsky,[∥,⊥] Wolfgang Haase,[⊥] Andrew Ozarowski,[#] Jerzy Krzystek,[#] Joshua Telser,[▽] Gerhard Schenk,[○] and Lawrence R. Gahan[○]

[†]*Departamento de Química, Universidade Federal de Santa Catarina, 88040-900 Florianópolis, SC, Brazil,* [‡]*Departamento de Bioquímica, Universidade Federal de Santa Catarina, 88040-900 Florianópolis, SC, Brazil,* [§]*Institute of Physics, Reymonta 4, Jagiellonian University, PL-30-059 Kraków, Poland,* [∥]*Institute of Applied Physics, Academy of Sciences of Moldova, Academy Str. 5, 2028 Chisinau, Moldava,* [⊥]*Institut für Physikalische Chemie, Technische Universität Darmstadt, Petersenstrasse 20, D-64287 Darmstadt, Germany,* [#]*National High Magnetic Field Laboratory, Florida State University, Tallahassee, Florida 32310,* [▽]*Department of Biological, Chemical and Physical Sciences, Roosevelt University, Chicago, Illinois 60605, and* [○]*School of Molecular and Microbial Sciences, The University of Queensland, St. Lucia, QLD 4072, Australia*

Received April 29, 2009

The design and development of suitable biomimetic catalytic systems capable of mimicking the functional properties of enzymes continues to be a challenge for bioinorganic chemists. In this study, we report on the synthesis, X-ray structures, and physicochemical characterization of the novel isostructural $[Fe^{III}Co^{II}(BPBPMP)(\mu\text{-}OAc)_2]ClO_4$ (**1**) and $[Ga^{III}Co^{II}(BPBPMP)(\mu\text{-}OAc)_2]ClO_4$ (**2**) complexes with the unsymmetrical dinucleating ligand $H_2BPBPMP$ (2-bis[{(2-pyridyl-methyl)-aminomethyl}-6-{(2-hydroxy-benzyl)-(2-pyridyl-methyl)}-aminomethyl]-4-methylphenol). The previously reported complex $[Fe^{III}Zn^{II}(BPBPMP)(\mu\text{-}OAc)_2]ClO_4$ (**3**) was investigated here by electron paramagnetic resonance for comparison with such studies on **1** and **2**. A magneto-structural correlation between the exchange parameter J (cm^{-1}) and the average bond lengh d (Å) of the $[Fe^{III}-O-M^{II}]$ structural unit for **1** and for related isostructural $Fe^{III}M^{II}$ complexes using the correlation $J = -10^7 \exp(-6.8d)$ reveals that this parameter is the major factor that determines the degree of antiferromagnetic coupling in the series $[(BPBPMP)Fe^{III}(\mu\text{-}OAc)_2M^{II}]^+$ (M^{II} = Mn, Fe, Co, Ni) of complexes. Potentiometric and spectrophotometric titrations along with electronic absorption studies show that, in aqueous solution, complexes **1** and **2** generate the $[(HO)M^{III}(\mu\text{-}OH)Co^{II}(H_2O)]$ complex as the catalytically active species in diester hydrolysis reactions. Kinetic studies on the hydrolysis of the model substrate bis(2,4-dinitrophenyl)phosphate by **1** and **2** show Michaelis–Menten behavior, with **2** being 35% more active than **1**. In combination with k_H/k_D isotope effects, the kinetic studies suggest a mechanism in which a terminal M^{III}-bound hydroxide is the hydrolysis-initiating nucleophilic catalyst. In addition, the complexes show maximum catalytic activity in DNA hydrolysis near physiological pH. The modest reactivity difference between **1** and **2** is consistent with the slightly increased nucleophilic character of the $Ga^{III}-OH$ terminal group in comparison to $Fe^{III}-OH$ in the dinuclear $M^{III}Co^{II}$ species.

Introduction

Proteins containing dinuclear metal centers in their active sites are well-characterized and encompass a wide range of biological functions.[1−4] Purple acid phosphatases (PAPs) are nonspecific phosphomonoesterases, which have been isolated from mammal, plant, and fungal sources.[2,5] The dinuclear metal core of these enzymes reveals an $Fe^{III}M^{II}$ motif where M^{II} can be Fe, Zn, or Mn ions. They are distinguished from other acid phosphatases by their purple color, due to a tyrosinate → Fe^{III} charge-transfer transition at around 560 nm,

*To whom correspondence should be addressed. Tel.: +55 48 3721-6844 r219. Fax: +55 48 3721-6850. E-mail: ademir@qmc.ufsc.br.

(1) Twitchett, M. B.; Sykes, A. G. *Eur. J. Inorg. Chem.* **1999**, 2105.
(2) (a) Mitić, N.; Smith, S. J.; Neves, A.; Guddat, L. W.; Gahan, L. R.; Schenk, G. *Chem. Rev.* **2006**, *106*, 3338. (b) Gahan, L. R.; Smith, S. J.; Neves, A.; Schenk, G. *Eur. J. Inorg. Chem.* **2009**, 2745.
(3) Sträter, N.; Lipscomb, W. N.; Klabunde, T.; Krebs, B. *Angew. Chem., Int. Ed. Engl.* **1996**, *35*, 2024.
(4) Vincent, J. B.; Olivier-Lilley, G. L.; Averill, B. A. *Chem. Rev.* **1990**, *90*, 1447.
(5) Chen, T. T.; Baser, F. W.; Cetorelli, J. J.; Pollard, W. E.; Roberts, R. M. *J. Biol. Chem.* **1973**, *248*, 8560.

Published on Web 07/15/2009

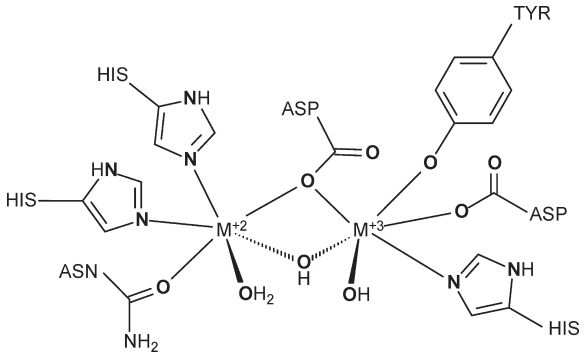

Figure 1. Common dinuclear active site for the animal and plant PAPs where M^{III} is Fe and M^{II} can be Mn, Fe, or Zn.

and by their insensitivity to L-tartarate, which is an inhibitor of other classes of acid phosphatases.[2,5−9] Despite the fact that their physiological roles are not yet well-defined, PAPs are efficient catalysts for the *in vitro* hydrolysis of a wide range of activated phosphoric acid esters and anhydrides, such as ATP, at a pH range from 4 to 7.[10−19] The crystal structures of PAPs from several biological sources have been determined.[2,8−12] Despite low overall protein sequence homology, all PAPs contain highly conserved active sites with seven invariant amino acid residues coordinating the dinuclear metal sites.[20] The Fe^{III} ion is coordinated by a tyrosine, a histidine, and a monodentate aspartate, while the divalent M^{II} has two histidines and an asparagine ligand. The two metal ions are μ-1,1-bridged by an aspartate. In order to complete the coordination spheres, exogenous ligands, such as a μ-hydroxo intermetallic bridge (a terminal aqua for M^{II} and a terminal hydroxo for Fe^{III}), were modeled[8] on the basis of spectroscopic,[16] magnetic,[17] and electrochemical[18] measurements. A monodentate bridging carboxylate group of an aspartate residue completes the coordination spheres of the Fe^{III} and M^{II} centers. Figure 1 shows a general scheme of the common active site for the PAPs.

It is important to emphasize that the two chemically distinct coordination environments around the metal centers are essential for the catalytic properties of this enzyme, though their individual roles remain a matter of debate. In the initially proposed model for the mechanism of PAP-catalyzed reactions, the phosphate group of the substrate binds to, and is orientated and activated by, the divalent metal ion, while an Fe^{III}-bound hydroxide group attacks "in line" the electrophilic phosphorus atom of the substrate, thus initiating ester bond hydrolysis.[2,8] Recently, a mechanism in which the μ-OH(O) bridge is appropriately oriented and acts as the nucleophile for hydrolysis has also been proposed for some PAPs.[15,19,21]

In order to probe the role of the metal ions in enzymatic catalysis, the effect of metal ion substitutions on reactivity has been studied. The divalent metal ion in both pig and red kidney bean PAPs can be replaced by a range of metal ions (including Co, Cu, Zn, Cd, Ni, and Hg), resulting in derivatives that exhibit activities varying from 20% to 100% of that of the native enzyme.[22−26] Similar observations have also been made with bovine spleen PAP (bsPAP).[27] Furthermore, the Fe^{III} center has been replaced by Ga^{III} to produce $Ga^{III}Fe^{II}$ and $Ga^{III}Zn^{II}$ in pig PAP and bsPAP. These derivatives exhibit catalytic activities similar to those of the native $Fe^{III}Fe^{II}$ forms, providing evidence that diamagnetic Ga^{III} can act as a functional analog of paramagnetic Fe^{III}.[26−29] The replacement of both Fe^{II} and Fe^{III} of bsPAP to give fully diamagnetic $Al^{III}Zn^{II}$ and $In^{III}Zn^{II}$ derivatives has also been carried out, but the latter is catalytically inactive.[30]

In parallel with the above enzymatic studies, the study of heterodinuclear mixed-valence small molecules is interesting with regard to their potential in modeling the structure and reactivity of the corresponding metalloenzymes. However, the preparation of mixed-metal complexes is often a considerable challenge.[31] Heterodinuclear $M^{III}M^{II}$ complexes, which are able to reproduce the structural, spectroscopic, and functional properties of PAPs, can be very useful in evaluating the conflicting proposed mechanisms of these metalloenzymes. Indeed, we have successfully developed a general method for the preparation of mixed-valence homo- and heterodinuclear $M^{III}M^{II}$ complexes, using the unsymmetrical

(6) Beck, J. L.; McConachie, L. A.; Summers, A. C.; de Jersey, J.; Zerner, B. *Biochim. Biophys. Acta* **1986**, *869*, 61.
(7) Ullah, A. H. J.; Mullaney, E. M.; Dischinger, H. C., Jr. *Biochem. Biophys. Res. Commun.* **1994**, *203*, 182.
(8) Klabunde, T.; Sträter, N.; Fröhlich, R.; Witzel, H.; Krebs, B. *J. Mol. Biol.* **1996**, *259*, 737.
(9) Oddie, G. W.; Schenk, G.; Angel, N. Z.; Walsh, N.; Guddat, L. W.; de Jersey, J.; Cassady, A. I.; Hamilton, S. E.; Hume, D. A. *Bone* **2000**, *27*(5), 575.
(10) Klabunde, T.; Krebs, B. *Struct. Bonding* (*Berlin*) **1997**, *89*, 177.
(11) Uppenberg, J.; Lindqvist, F.; Svensson, B.; Ek-Rylander, B.; Andersson, G. *J. Mol. Biol.* **1999**, *290*, 201.
(12) Lindqvist, Y.; Johansson, E.; Kaija, H.; Vihko, P.; Schneider, G. *J. Mol. Biol.* **1999**, *291*, 135.
(13) Guddat, L. W.; McAlpine, A. S.; Hume, D.; Hamilton, S.; Jersey, J.; Martin, J. L. *Structure* **1999**, *7*, 757.
(14) Schenk, G.; Boutchard, C. L.; Carrington, L. E.; Noble, C. J.; Moubaraki, B.; Murray, K. S.; de Jersey, J.; Hanson, G. R.; Hamilton, S. *J. Biol. Chem.* **2001**, *276*, 19084.
(15) Schenk, G.; Ge, Y.; Carrington, L. E.; Wynne, C. J.; Searle, I. R.; Carrol, B. J.; Hamilton, S.; de Jersey, J. *Arch. Biochem. Biophys.* **1999**, *370*, 183.
(16) Smoukov, S. K.; Quaroni, L.; Wang, X.; Doan, P. E.; Hoffman, B. M.; Que, L., Jr. *J. Am. Chem. Soc.* **2002**, *124*, 2595.
(17) Averill, B. A.; Davis, J. C.; Burman, S.; Zirino, T.; Sanders-Loehr, J.; Loehr, T. M.; Sage, J. T.; Debrunner, P. G. *J. Am. Chem. Soc.* **1987**, *109*, 3760.
(18) Wang, D. L.; Holz, R. C.; David, S. S.; Que, L., Jr.; Stankovich, M. *Biochem.* **1991**, *30*, 8187.
(19) Cox, R. S.; Schenk, G.; Mitić, N.; Gahan, L. R.; Henge, A. *J. Am. Chem. Soc.* **2007**, *129*, 9550.
(20) Schenk, G.; Korsinczky, M. L. J.; Hume, D. A.; Hamilton, S.; de Jersey, J. *Gene* **2000**, *255*, 419.
(21) Schenk, G.; Gahan, L. R.; Carrington, L. E.; Mitić, N.; Valizadeh, M.; Hamilton, S. E.; de Jersey, J.; Gudat, L. W. *PNAS* **2005**, *102*, 273.
(22) Keough, D. T.; Dionysius, D. A.; de Jersey, J.; Zerner, B. *Biochem. Biophys. Res. Commun.* **1980**, *94*, 600.
(23) Beck, J. L.; Keough, D. T.; de Jersey, J.; Zerner, B. *Biochim. Biophys. Acta* **1984**, *791*, 357.
(24) Beck, J. L.; de Jersey, J.; Zerner, B.; Hendrich, M. P.; Debrunner, P. G. *J. Am. Chem. Soc.* **1988**, *110*, 3317.
(25) Beck, J. L.; McArthur, M. J.; de Jersey, J.; Zerner, B. *Inorg. Chim. Acta* **1988**, *153*, 39.
(26) Schenk, G.; Peralta, R. A.; Batista, S. C.; Bortoluzzi, A. J.; Szpoganicz, B.; Dick, A. K; Herrald, P.; Hanson, G. R; Szilagyi, R. K; Riley, M. J.; Gahan, L. R.; Neves, A. *J. Biol. Inorg. Chem.* **2008**, *13*, 139.
(27) (a) Davis, J. C.; Averill, B. A. *PNAS* **1982**, *79*, 4623. (b) David, S. S.; Que, L., Jr. *J. Am. Chem. Soc.* **1990**, *112*, 6455.
(28) Merkx, M.; Averill, B. A. *Biochem.* **1998**, *37*, 8490.
(29) Smith, S. J.; Casellato, A.; Hadler, K. S.; Mitić, N.; Riley, M. J.; Bortoluzzi, A. J.; Szpoganicz, B.; Schenck, G.; Neves, A.; Gahan, L. *J. Biol. Inorg. Chem.* **2007**, *12*, 1207.
(30) Merkx, M.; Averill, B. A. *J. Am. Chem. Soc.* **1999**, *121*, 6683.
(31) Ghiladi, M.; McKenzie, C. J.; Meier, A.; Powell, A. K.; Ulstrup, J.; Wocadlo, S. *J. Chem. Soc., Dalton Trans.* **1997**, 4011.

H_2BPBPMP ligand.[29,26−40] Herein, we report two novel heterodinuclear complexes, $[Fe^{III}Co^{II}(BPBPMP)(\mu\text{-}OAc)_2]ClO_4$ (**1**) and $[Ga^{III}Co^{II}(BPBPMP)(\mu\text{-}OAc)_2]ClO_4$ (**2**), with a single terminal $M^{III}-O_{phenolate}$ bond as a selected motif in order to mimic some structural and functional properties of substituted PAPs. To the best of our knowledge, **1** and **2** represent the first example of complexes containing the $[M^{III}(\mu\text{-}O_{phenoxo})(\mu\text{-}OAc)_2Co^{II}]$ (M^{III} = Fe, Ga) moiety to be structurally characterized. Both complexes have been thoroughly investigated by spectroscopic and reactivity studies. For completeness, we also studied by EPR the Zn^{II} analog to **1**, $[Fe^{III}Zn^{II}(BPBPMP)(\mu\text{-}OAc)_2]ClO_4$ (**3**). Both $M^{III}Co^{II}$ complexes, **1** and **2**, show significant catalytic efficiency toward the hydrolytic cleavage of the activated substrate bis(2,4-dinitrophenyl)phosphate (2,4-BDNPP) and of DNA itself.

Experimental Section

Abbreviations. The following abbreviations are used in this paper: PAPs, purple acid phosphatases; Uf, uteroferrin (pigPAP); bsPAP, bovine spleen PAP; rkbPAP, red kidney bean PAP; spPAP, sweet potato PAP; rbTRAP, rat bone tartarate-resistant acid phosphatase; H_2BPBPMP, 2-bis{[(2-pyridylmethyl)aminomethyl]-6-[(2-hydroxybenzyl)(2-pyridylmethyl)]-aminomethyl}-4-methylphenol; CT-DNA, calf thymus DNA; CHES, 2-(cyclohexylamino)-ethanesulfonic acid; HEPES, 2-[4-(2-hydroxyethyl)-1-piperazine]-ethanesulfonic acid; MES, 2-[*N*-morpholine]ethanesulfonic acid; 2,4-BDNPP, bis(2,4-dinitrophenyl)phosphate; 2,4-DNPP, 2,4-dinitrophenylphosphate; 2,4-DNP, 2,4-dinitrophenolate; ph, phenolate; P_i, inorganic phosphate; E_{pa}, anodic peak potential; *f*, catalytic factor; *J*, magnetic exchange coupling constant; K_{assoc}, association constant; k_{cat}, catalytic constant; K_M, Michaelis−Menten constant; *n*-Bu_4NPF_6, tetra-*n*-butylammonium hexafluorophosphate; HFEPR, high-frequency and -field electron paramagnetic resonance; MCD, magnetic circular dichroism; NHE, normal hydrogen electrode; LMCT, ligand-to-metal charge transfer; ZFS, zero-field splitting.

Materials, Instrumentation, and Procedures. All reagents of high-purity grade were purchased from commercial sources and used as received. In the characterization of the complexes and in the kinetics studies, spectroscopic-grade solvents from Merck, dried using molecular sieves, were used.

Elemental Analysis. C, H, and N determinations were performed on a Carlo Erba model E-1110 analyzer.

Conductometric Measurements. The molar conductivities of **1** and **2** were evaluated in a Schott-Geräte CG 853 conductivimeter at room temperature using a 0.001 M spectroscopic-grade acetonitrile solution.

Electrochemistry. The electrochemical behavior of **1** and **2** was investigated with a Princeton Applied Research (PARC) 273 potentiostat/gavanostat. Cyclic and square-wave voltammograms were obtained at room temperature in acetonitrile solutions containing 0.1 M *n*-Bu_4NPF_6 as a supporting electrolyte under an argon atmosphere. The electrochemical cell employed was comprised by three electrodes: platinum (working), platinum wire (auxiliary), and Ag/Ag^+ (reference). The ferrocene/ferrocenium couple Fc/Fc^+ ($E^{1/2}$ 372 mV vs Ag/Ag^+; E^0 = 400 mV vs NHE) was used as the internal standard.[41]

Magnetochemistry. DC magnetization data were obtained with a SQUID magnetometer on polycrystalline samples of complex **1**. The sample was pressed into a pellet in order to avoid the reorientation of the particles in the external magnetic field. The data were corrected for the diamagnetic core contribution as deduced with the use of Pascal's constant tables.[42]

The values of the magnetization and the magnetic susceptibility for an arbitrary direction of the applied magnetic field can be calculated as

$$M(\vartheta,\varphi) = N_A k_B T \frac{\partial}{\partial H(\vartheta,\varphi)}\{\ln Z[H(\vartheta,\varphi)]\} \qquad (1)$$

$$\chi(\vartheta,\varphi) = M(\vartheta,\phi)/H(\vartheta,\phi)$$

Z is the partition function, and k_B and N_A are Boltzmann's constant and Avogadro's number, respectively. The powder averaged magnetic susceptibility can be calculated as χ_{av}= 1/3-($\chi_x + \chi_y + \chi_z$), whereas for the calculation of magnetization the averaging over all possible orientations of the external magnetic field should be performed.

EPR Spectroscopic Measurements and Analysis. HFEPR spectra were recorded using both the Millimeter and Submillimeter Wave Facility and the EMR Facility at NHMFL. The former experimental setup employs backward wave oscillators generating tunable frequencies in the 70 GHz to 1.2 THz range (of which the 120−700 GHz range was used in this study) and the resistive "Keck" magnet enabling 0−25 T field sweeps,[43] while the latter utilizes a variety of solid-state sources and a superconducting 15/17 T magnet.[44] Detection was provided with an InSb hot-electron bolometer (QMC Ltd., Cardiff, U.K.). Modulation for detection purposes was provided alternatively by chopping the sub-terahertz wave beam ("optical modulation"), which produced an absorptive shape of the spectra, or by modulating the magnetic field, which delivered the more standard first derivative shape. A Stanford Research Systems SR830 lock-in amplifier converted the modulated signal to DC voltage. A typical size of a polycrystalline sample was 20−40 mg. EPR spectra at 35 GHz for **2** in a 1:1 v/v acetonitrile/toluene solution (2 mM) were recorded at 2 K on a modified Varian spectrometer.

The data for **1** ($Fe^{III}Co^{II}$ complex) were analyzed in terms a standard spin-Hamiltonian for $S = 1$ including zero-field splitting (ZFS) terms:

$$H = \beta_e B g S + D[S_Z^2 - (1/3)S(S+1)] + E[S_x^2 - S_Y^2] \qquad (2)$$

(32) (a) Neves, A.; Lanznaster, M.; Bortolozzi, A. J.; Peralta, R. A.; Casellato, A.; Castellano, E. E.; Herrald, P.; Riley, M. J.; Schenk, G. *J. Am. Chem. Soc.* **2007**, *129*, 7486. (b) Ferreira, D. E. C.; Almeida, W. B. D.; Neves, A.; Rocha, W. R. *Phys. Chem. Chem. Phys.* **2008**, *10*, 7039.
(33) Lanznaster, M.; Neves, A.; Bortoluzzi, A. J.; Szpoganicz, B.; Schwingel, E. *Inorg. Chem.* **2002**, *41*, 5641.
(34) Neves, A.; de Brito, M. A.; Drago, V.; Griesar, K.; Haase, W. *Inorg. Chim. Acta* **1995**, *237*, 131.
(35) Karsten, P.; Neves, A.; Bortoluzzi, A. J.; Strähle, J.; Maichle-Mössmer, C. *Inorg. Chem. Commun.* **2002**, *5*, 434.
(36) Horn., Jr., A. Ph.D. Thesis, Federal University of Santa Catarina, Santa Catarina, Brazil, **2000**.
(37) Karsten, P.; Neves, A.; Bortoluzzi, A. J.; Drago, V.; Lanznaster, M. *Inorg. Chem.* **2002**, *41*, 4624.
(38) Batista, S. C.; Neves, A.; Bortoluzzi, A. J.; Vencato, I.; Peralta, R. A.; Szpoganicz, B.; Aires, V. E.; Severino, P. A. *Inorg. Chem. Commun.* **2003**, *6*, 1161.
(39) Lanznaster, M.; Neves, A.; Bortoluzzi, A. J.; Aires, V. V. E.; Szpoganicz, B.; Terenzi, H.; Severino, R. C.; Fuller, J. M.; Drew, S. C.; Gahan, L. R.; Hanson, G. R.; Riley, M. J.; Schenk, G. *J. Biol. Inorg. Chem.* **2005**, *10*, 319.
(40) Neves, A.; de Brito, M.; Vencato, I.; Drago, V.; Griesar, K.; Haase, W. *Inorg. Chem.* **1996**, *35*, 2360.
(41) Gagné, R. R.; Koval, C. A.; Lisensky, G. C. *Inorg. Chem.* **1980**, *19*, 2854.
(42) Carlin, R. L. *Magnetochemistry*; Springer-Verlag: Berlin, 1986.
(43) Zvyagin, S. A.; Krzystek, J.; van Loosdrecht, P. H. M.; Dhalenne, G.; Revcolevschi, A. *Physica B* **2004**, *346−347*, 1.
(44) Hassan, A. K.; Pardi, L. A.; Krzystek, J.; Sienkiewicz, A.; Goy, P.; Rohrer, M.; Brunel, L.-C. *J. Magn. Reson.* **2000**, *142*, 300.

where D and E are the axial and rhombic second-order ZFS parameters, respectively. Turning points in the powder spectra were plotted as a function of the operating frequency to produce a 2-D field/frequency map and the spin-Hamiltonian parameters best-fitted to it.[45] The fitting software also generates simulations of single-frequency spectra. The data for **2** ($Ga^{III}Co^{II}$ complex) were analyzed in terms of the effective $S' = 1/2$ spin Hamiltonian, $H_{eff} = \beta_e B g S$, using the same tunable-frequency methodology as for **1**. The data for **3** ($Fe^{III}Zn^{II}$ complex) were interpreted using single-frequency spectra and the same spin-Hamiltonian as for **1** (eq 2), except for $S = 5/2$. Higher-order ZFS and Zeeman terms were not considered, although they are possible for $S = 5/2$.[46]

Magnetic Circular Dichoism (MCD) Spectroscopy. MCD spectra of **1** and **2** complexes were collected by means of a JASCO J-810 spectropolarimeter, interfaced with an Oxford Instruments Spectromag SM 4000-9T cryostat. The samples were ground, and the obtained fine powder was mixed with Nujol. The MCD spectra were corrected for the natural circular dichroism and other baseline effects by subtracting the background line at 0 T. Spectra were measured for various temperatures (3 K and above) and at each temperature for various magnetic fields from 0 up to 8 T.

IR and UV−Vis Spectroscopic Measurements. Infrared spectra were collected on a Perkin-Elmer 1600 spectrometer using KBr pellets in the range of 4000−500 cm^{-1}. Electronic spectra of **1** and **2** in the range 300−900 nm were recorded with a Perkin-Elmer L19 spectrophotometer at room temperature with quartz cells. Spectroscopic-grade acetonitrile was used as the solvent. The spectra of the complexes in kinetic conditions were carried out under the following conditions: MeCN/H_2O (50% v/v); pH 7.0; HEPES buffer, 0.1 M; ionic strength ($LiClO_4$), 0.05 M; [complex] = 4.0×10^{-5} M. Values of ε are given in $M^{-1}\,cm^{-1}$. The solid-state experiments (diffuse reflectance) were performed in KBr dispersion pellets.

Potentiometric Titration. The protonation constants for complexes **1** and **2** were investigated with a Corning 350 pH meter fitted with a glass-combined electrode (Ag/AgCl) calibrated to read −log [H^+] directly, designated as pH. The experiment temperature was stabilized at 25.00 ± 0.05 °C. Doubly distilled water in the presence of $KMnO_4$ was used to prepare CH_3CN/H_2O (50/50 v/v) solutions. The electrode was calibrated using the data obtained from a titration of a known volume of a standard 0.0100 M HCl solution with a standard 0.100 M KOH solution. The ionic strength was kept constant at 0.1 M by the addition of KCl, and the solutions, containing 0.05 mmol of the complex, were titrated with 0.100 M standard CO_2-free KOH. Experiments were performed in 50.00 mL water/ethanol solutions in a thermostatted cell, purged with argon cleaned using two 0.1 M KOH solutions. The experiments were performed at least in triplicate and were all analyzed using the BEST7 program.[47] The species diagrams were obtained with SPE[47] and SPEPLOT[47] programs.

Kinetics Measurements. The phosphatase-like activity of **1** and **2** toward the activated phosphoric diester 2,4-BDNPP[48] and monoester 2,4-DNPP[49] was evaluated spectrophotometrically on a Varian Cary50 Bio spectrophotometer, at 400 nm, by the appearance of the 2,4-dinitrophenolate ion at 25 °C. The pH effect on the hydrolytic cleavage of 2,4-BDNPP was monitored in the pH range from 3.5 to 11.0. Reactions were performed using the following conditions: 1.5 mL of a freshly prepared aqueous buffer solution ($[B]_{final}$ 5.00×10^{-2} M); buffer = MES (pH 3.50−6.50), HEPES (pH 7.00−8.50), CHES (pH 9.00−10.00), and CAPS (pH 10.50−11.00) with controlled ionic strength ($LiClO_4$), 0.05 M; 200 μL of an acetonitrile complex solution ($[C]_{final} = 4.00 \times 10^{-5}$ M) and 500 μL of acetonitrile were added to a 1-cm-path-length cell. The reaction was initiated by the addition of 800 μL of an acetonitrile substrate solution ($[S]_{final} = 8.50 \times 10^{-3}$ M) and monitored between 2 and 5% of reaction at 25 °C. The kinetic experiments under conditions of an excess of the substrate were performed as follows: 1.5 mL of a freshly prepared aqueous buffer HEPES solution (at pH 7.00), $[B]_{final} = 5.00 \times 10^{-2}$ M, and 200 μL of an acetonitrile complex solution ($[C]_{final} = 4.00 \times 10^{-5}$ M) were added to a 1-cm-path-length cell. The reaction was initiated with the addition of volumes from 160 to 1280 μL of a 2,4-BDNPP solution ($[2,4\text{-BDNPP}]_{final} = 1.00 \times 10^{-3}$ to 8.00×10^{-3} M). Correction for the spontaneous hydrolysis of the 2,4-BDNPP was carried out by direct difference using a reference cell under identical conditions without adding the catalyst. The initial rate was obtained from the slope of the absorbance versus time plot over the first 5 min of reaction. The conversion of the reaction rate units was carried out using $\varepsilon = 12\,100\ M^{-1}\,cm^{-1}$ for 2,4-DNP and the initial concentration of the complex.[35−38] A kinetic treatment using the Michaelis−Menten approach was applied, and the results were evaluated from Lineweaver−Burk plots. The deuterium isotopic effect on the hydrolytic process was evaluated following two reactions with identical conditions (vide pH effect experiments) using a HEPES buffer (pH or pD 7.00, previously prepared) and a 125-fold excess of the substrate in comparison to the complex concentration. The reactions were monitored at 400 nm and 25 °C. Measurements of the inhibitory effect of acetate anions in the cleavage of 2,4-BDNPP were performed using a 100-fold excess of the substrate ($[2,4\text{-BDNPP}]_{final} = 4.0 \times 10^{-3}$ M, $[C]_{final} = 4.0 \times 10^{-5}$ M, and NaOAc [I] = 2.68×10^{-2} M). The reaction was initiated by the addition of volumes from 0 to 170 μL of a buffer/NaOAc solution ($[NaOAc]_{final}$ ranging 0 to 1.6×10^{-3} M).

DNA Cleavage. Plasmid DNA cleavage experiments were carried out at different concentrations of metal complexes (complexes **1** and **2**) with 680 ng (40 μM DNA base pairs (bp)) of pBSK-II plasmid DNA, in a final volume of 20 μL. Samples were incubated for 16 h at 37 °C, with 5 mM PIPES ($I = 0.01$ M); at a pH of 6.0, 6.5, and 7.0; and with 25% acetonitrile (v/v) with a final complex concentration of 5, 20, or 40 μM. Samples were submitted to agarose gel electrophoresis and stained with ethidium bromide. The resulting gels were digitalized with a photodocumentation system (UVP Inc., Upland, CA), and DNA bands were quantified using LabWorks software, version 4.0 (UVP).[50,51] In order to verify complex/DNA interaction, UV−vis spectra of complex **1** were recorded in the presence of increasing amounts of calf thymus DNA (CT-DNA). Reactions were performed in a volume of 400 μL, and final concentrations were 5 mM PIPES at a pH of 6.0 ($I = 0.01$ M), acetonitrile 25% (v/v), and 40 μM complex **1**. Spectra data of reactions with increasing values of [CT-DNA]/[complex] (R) were evaluated by following the changes in the maximum absorbance and shifts in maximum absorption wavelength, using an Ultrospec 2100 Pro (Amersham Biosciences). The intrinsic binding constant (K_b) of complex **1** with the CT-DNA was derived from these data.[38,50,51]

Syntheses of the Complexes. Synthesis of 1. Complex **1** was synthesized by the addition of $Co^{II}(OAc)_2 \cdot 4H_2O$ (0.124 g, 0.5 mmol) to a methanolic solution of the $H_2BPBPMP$[37] ligand

(45) Krzystek, J.; Ozarowski, A.; Telser, J. *Coord. Chem. Rev.* **2006**, *250*, 2308. (b) Krzystek, J.; Zvyagin, S. A.; Ozarowski, A.; Trofimenko, S.; Telser, J. *J. Magn. Reson.* **2006**, *178*, 174.
(46) Abragam, A.; Bleaney, B. *Electron Paramagnetic Resonance of Transition Ions*; Dover Publications, Inc.: New York, 1986.
(47) Martell A. E.; Motekaitis, R. J *Determination of Stability Constants*, 2nd ed.; VHC Publishers: Weinheim, Germany, 1992.
(48) Bunton, C. A.; Farber, S. J. *J. Org. Chem.* **1969**, *34*, 767.
(49) Rawji, G.; Milburn, R. M. *J. Org. Chem.* **1981**, *46*, 1205.
(50) (a) Oliveira, M. C. B.; Scarpellini, M.; Neves, A.; Terenzi, H.; Bortoluzzi, A. J.; Szpoganicz, B.; Greatti, A.; Mangrich, A. S.; Souza, E. M.; Fernandez, P. M.; Soares, M. *Inorg. Chem.* **2005**, *44*, 921–929. (b) Weston, J. *Chem. Rev.* **2005**, *105*, 2151.
(51) (a) Hopkins, A. L.; Mason, J. S.; Overington, J. P. *Curr. Opin. Struct. Biol.* **2006**, *16*, 127. (b) Hult, K.; Berglund, P. *Trends Biotechnol.* **2007**, *25*, 231.

Table 1. Summary of Crystallographic Data for Complexes **1** and **2**

	complex 1	complex 2
empirical formula	$C_{38}H_{39.50}ClCoFeN_5O_{10.25}$	$C_{38}H_{41}ClCoGaN_5O_{11}$
fw	880.48	907.86
temperature (*K*)	293(2)	293(2)
wavelength λ Mo Kα (Å)	0.71069	0.71069
cryst syst	monoclinic	monoclinic
space group	$P2_1/c$	$P2_1/n$
a (Å)	19.612(3)	12.651(2)
b (Å)	10.795(1)	18.191(4)
c (Å)	20.807(4)	16.857(6)
β (deg)	116.67(1)	93.74(2)
volume (Å^3)	3936.4(11)	3871.1(17)
Z	4	4
ρ_{calcd} (g cm^{-3})	1.486	1.558
μ (mm^{-1})	0.922	1.261
F (000)	1818	1868
abs correction	ψ-scan	ψ-scan
transm. factors (T_{max} and T_{min})	0.628 and 0.596	0.821 and 0.587
reflns	7144	7101
unique	6928 (R_{int} = 0.0804)	6857 (R_{int} = 0.0247)
params/restraints	528/113	535/113
GOF (F^2)	1.060	1.043
$R(F)$ ($I > 2\sigma(I)$)	0.0612	0.0383
$R_w(F^2)$ (all data)	0.1753	0.0991

(0.273 g, 0.5 mmol), followed by the dropwise addition of a methanolic solution of $Fe^{III}(ClO_4)_3 \cdot 9H_2O$ (0.258 g, 0.5 mmol). The mixture was maintained under magnetic stirring, at 40 °C, for 20 min. Finally, 0.0820 g (1.0 mmol) of NaOAc was added. The solution immediately turned purple, and after 24 h, purple crystals suitable for X-ray analysis were isolated. Yield: 66% (0.264 g, 0.3 mmol). Anal. Calcd for $C_{38}H_{43}ClCoFeN_5O_{12}$, fw = 912.02 g mol^{-1}: C, 50.04; H, 4.75; N, 7.68. Found: C, 49.75; H, 4.63; N, 7.55%. IR: ν_{ass}(COO) 1580 cm^{-1}, ν_s(COO) 1430 cm^{-1}, ν(C−O_{ph}) 1300 cm^{-1}, $\nu(ClO_4)$ 1095 cm^{-1}. Molar conductivity: 140 Ω^{-1} mol^{-1} cm^2.

Synthesis of 2. Complex **2** was prepared in a similar way to complex **1** by the addition of $Co^{II}(OAc)_2 \cdot 4H_2O$ (0.124 g, 0.5 mmol) to a methanolic solution of the H_2BPBPMP[37] ligand (0.273 g, 0.5 mmol), followed by the drop-by-drop addition of a methanolic solution of $Ga^{III}(NO_3)_3$ (0.128 g, 0.5 mmol). The mixture was maintained under magnetic stirring, at 40 °C and for 20 min. Finally, 0.0820 g (1.0 mmol) of NaOAc and 0.122 g (1.0 mmol) of $NaClO_4$ were added. After 10 min, a brownish solid was isolated and recrystallized from ethanol. After 24 h, brown crystals suitable for X-ray analysis were isolated. Yield: 42% (0.190 g, 0.2 mmol). Anal. Calcd for $C_{38}H_{41}ClCoGaN_5O_{11}$, fw = 907.86 g mol^{-1}: C, 50.27; H, 4.55; N, 7.71. Found: C, 50.30; H, 4.56; N, 7.58%. IR: ν_{ass}(COO) 1575 cm^{-1}, ν_s(COO) 1435 cm^{-1}, ν(C−O_{ph}) 1320 cm^{-1}, $\nu(ClO_4)$ 1095 cm^{-1}. Molar conductivity: 128 Ω^{-1} mol^{-1} cm^2.

Caution! *Perchlorate salts of metal complexes are potentially explosive and therefore should be prepared in small quantities.*

Complex 3. The complex $[Fe^{III}Zn^{II}(BPBPMP)(\mu\text{-}OAc)_2]ClO_4$ was synthesized as previously described.[33]

X-Ray Crystallography. For both complexes, the intensity data were collected with an Enraf-Nonius CAD4 diffractometer with graphite-monochromated Mo Kα radiation, at room temperature. Cell parameters were determined from 25 carefully centered reflections using a standard procedure.[52a] The intensities were collected using ω-2θ scan technique. All data were corrected for Lorentz and polarization effects.[52b] An empirical absorption correction based on the azimuthal scans of seven appropriate reflections was also applied to the collected intensities with the PLATON program.[52c] The structure was solved by direct methods and refined by full-matrix least-squares methods using SIR97[52d] and SHELXL97[52e] programs, respectively.

Complex 1. A dark red crystal was selected from the crystalline sample of complex **1** under polarized light and fixed at the end of a glass fiber for X-ray analysis. Most non-hydrogen atoms were refined anisotropically. The exception was for the water molecule, which was refined isotropically with a site occupancy of 0.25, and its H atoms were not located from Fourier difference maps. H atoms attached to C atoms were placed at their idealized positions, with C−H distances and U_{eq} values taken from the default settings of the refinement program. Two oxygen atoms of the perchlorate group are disordered over two alternative positions with site occupancies of 0.63(2) and 0.34(2).

Complex 2. A pale yellow prismatic crystal was selected for X-ray analysis. All non-H atoms were refined with anisotropic displacement parameters. In this crystal structure, two oxygen atoms of the perchlorate counterion are also disordered with two alternative positions, being their refined occupancy factors of 0.62(2) and 0.38(2). Hydrogen atoms of the water molecule were found from Fourier maps and treated with a riding model. Hydrogen atoms bonded to carbon atoms were included in the refinement list using the same method as for complex **1**. Further relevant crystallographic data for complexes **1** and **2** are summarized in Table 1.

Crystallographic data of complexes **1** and **2** (atomic coordinates and equivalent isotropic displacement parameters, calculated hydrogen atom parameters, anisotropic thermal parameters, and bond lengths and angles) have been deposited at the Cambridge Crystallographic Data Center (deposition numbers CCDC 700902 and 700903). Copies of this information may be obtained free of charge from CCDC, 12 Union Road, Cambridge, CB2 1EZ, U.K. (fax, +44-1223-336-033; e-mail, deposit@ccdc.cam.ac.uk or http://www.ccdc.cam.ac.uk).

Results and Discussion

A wide variety of physical and chemical measurements have been performed on **1** and **2**. These include studies on the complexes both in the solid state and in fluid solution. The

(52) (a) *CAD-4 EXPRESS*, version 5.1/1.2; Enraf-Nonius: Delft, The Netherlands, 1994. (b) Spek, A. L. *HELENA*, CAD-4 Data Reduction Program; University of Utrecht, The Netherlands, 1996. (c) North, A. C. T.; Phillips, D. C.; Mathews, F. S. *Acta Crystallogr.* **1968**, *A24*, 351. Spek, A. L. *Acta Crystallogr.* **1990**, *A46*, C34. (d) Altomare, A.; Burla, M. C.; Camalli, M.; Cascarano, G. L.; Giacovazzo, C.; Guagliardi, A.; Moliterni, A. G. G.; Polidori, G.; Spagna, R. *J. Appl. Crystallogr.* **1999**, *32*, 115. (e) Sheldrick, G. M. *SHELXL 97*, Program for the Refinement of Crystal Structures; University of Göttingen: Göttingen, Germany, 1997.

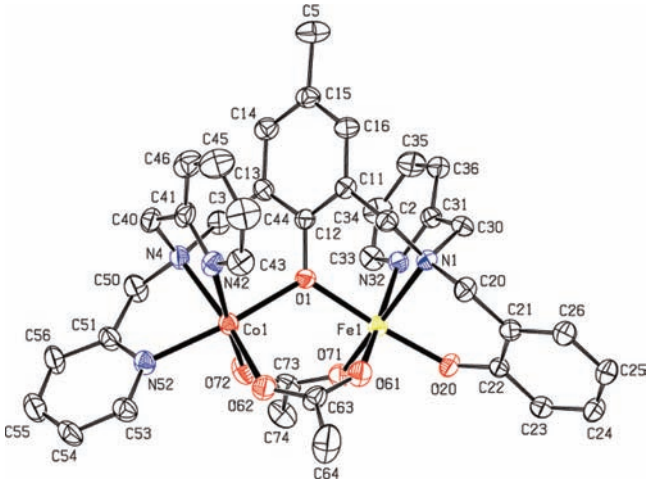

Figure 2. The molecular arrangement of the cation $[Fe^{III}Co^{II}(BPBPMP)(\mu\text{-}OAc)_2]^+$ (**1**).

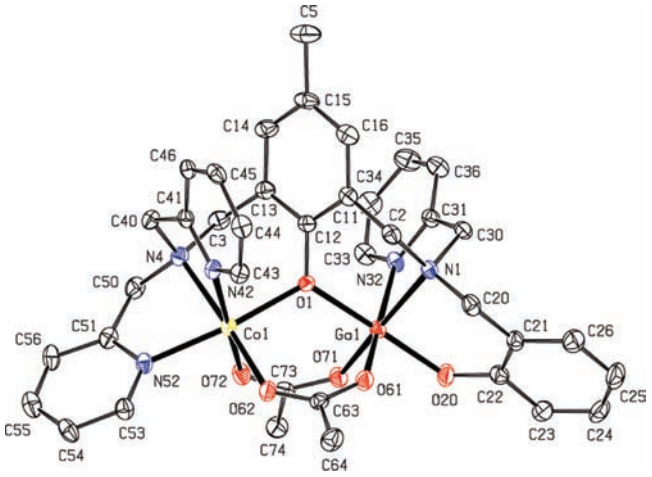

Figure 3. The molecular arrangement of the cation $[Ga^{III}Co^{II}(BPBPMP)(\mu\text{-}OAc)_2]^+$ (**2**).

former measurements include structure determination by X-ray crystallography as a starting point, magnetometric studies, and MCD and EPR spectroscopies. EPR measurements were also performed on the previously reported[33] analogous $Fe^{III}Zn^{II}$ complex, **3**, to provide information on the single-ion electronic properties of the magnetically isolated Fe^{III} site, just as EPR measurements on the $Ga^{III}Co^{II}$ complex **2** provide information on the Co^{II} site. Solution measurements on **1** and **2** include electronic absorption spectroscopy (diffuse reflectance spectra of solid samples were also recorded), electrochemistry, and potentiometric and spectrophotometric titrations, which demonstrate the acid/base properties of the complex that are crucial for catalytic hydrolysis. Last, to demonstrate the biomimetic relevance of these complexes, an extensive series of reactivity and kinetics studies was made of their phosphate ester hydrolysis and DNA cleavage properties.

Molecular Structures of 1 and 2. Well-formed purple crystals of **1** and brownish ones of **2** were characterized by single-crystal X-ray analysis, and their structures were solved. The atomic labeling schemes of **1** and **2** are shown in Figures 2 and 3, respectively. Selected bond lengths and angles are shown in Table 2.

Table 2. Selected Bond Lengths [Å] and Angles [deg] for Complexes **1** and **2**

	1	**2**
M^{III}–O20	1.888(3)	1.906(3)
M^{III}–O71	1.961(4)	1.934(3)
M^{III}–O1	2.014(3)	1.977(3)
M^{III}–O61	2.022(4)	1.988(3)
M^{III}–N32	2.175(4)	2.132(3)
M^{III}–N1	2.209(4)	2.143(3)
Co1–O62	2.040(4)	2.022(3)
Co1–O1	2.073(3)	2.052(3)
Co1–O72	2.125(4)	2.101(3)
Co1–N52	2.130(4)	2.096(3)
Co1–N42	2.156(5)	2.162(3)
Co1–N4	2.167(4)	2.170(3)
M^{III}–Co1	3.4892(12)	3.4840(13)
M^{III}–O1–Co1	117.24(16)	119.67(12)
O1–M^{III}–O61	89.73(15)	90.33(11)
O1–M^{III}–N32	85.75(14)	85.55(11)
O1–M^{III}–N32	85.75(14)	85.55(11)
O1–M^{III}–N1	88.21(14)	89.94(11)
O20–M^{III}–O71	92.05(15)	93.74(11)
O20–M^{III}–O1	174.68(15)	178.93(12)
O71–M^{III}–O1	93.15(14)	93.74(11)
O20–M^{III}–O61	90.56(16)	93.74(11)
O71–M^{III}–O61	98.99(17)	98.98(12)
O20–M^{III}–N32	93.12(16)	95.29(13)
O71–M^{III}–N32	90.21(16)	91.63(12)
O61–M^{III}–N32	169.97(17)	168.85(12)
O20–M^{III}–N1	86.47(15)	90.87(12)
O71–M^{III}–N1	167.73(15)	169.69(12)
O61–M^{III}–N1	93.21(16)	90.62(12)
N32–M^{III}–N1	77.72(15)	79.04(12)
O1–Co1–O72	88.45(14)	88.29(10)
O1–Co1–N52	164.98(16)	165.99(12)
O1–Co1–N42	87.13(15)	89.96(11)
O1–Co1–N4	90.65(15)	90.73(11)
O62–Co1–O1	96.65(15)	93.84(11)
O62–Co1–O72	93.32(18)	91.81(12)
O62–Co1–N52	95.82(17)	97.86(12)
O72–Co1–N52	82.50(16)	83.70(12)
O62–Co1–N42	95.94(18)	94.85(12)
O72–Co1–N42	170.15(17)	173.22(12)
N52–Co1–N42	99.87(17)	96.66(12)
O62–Co1–N4	171.41(16)	172.90(12)
O72–Co1–N4	91.39(17)	93.75(12)
N52–Co1–N4	77.67(16)	78.39(13)
N42–Co1–N4	79.86(17)	79.72(12)

Both crystal structures reveal a heterodinuclear $[M^{III}Co^{II}(BPBPMP)(\mu\text{-}OAc)_2]^+$ (with M^{III} = Fe or Ga) cation complex. The M^{III} and Co^{II} centers are bridged by the phenolate oxygen atom O1 of the $BPBPMP^{2-}$ ligand and by two exogenous carboxylate groups of the acetate ligands. Similarly to other $M^{III}M^{II}$ dinuclear model complexes containing the unsymmetrical $BPBPMP^{2-}$ ligand reported by Neves and co-workers,[26–40] the N_2O_4 coordination sphere of the trivalent center is completed by two nitrogen atoms (N1 and N32) of the tertiary amine and the pyridine atoms, respectively, and the O20 oxygen of the terminal phenolate (in the hard side of the ligand).[53] The N4, N42, and N52 nitrogen atoms of the tertiary amine and pyridine pendant arms complete the N_3O_3 octahedral coordination sphere of the Co1 center (soft side).[53] In **1**, the O62 and O72 oxygen atoms of the acetate groups are coordinated to Co1 in positions trans to the N4 tertiary amine and N42 pyridine nitrogen atoms, respectively, while another pyridine donor (N52) is in a

(53) Belle, C.; Gautier-Luneau, I.; Gellon, G.; Pierre, J. L.; Morgenstern-Badarau, I.; Saint-Aman, E. *J. Chem. Soc., Dalton Trans.* **1997**, 3543.

trans position to the oxygen O1 from the μ-phenoxo bridge. The O61 and O71 oxygen atoms of the acetate groups are coordinated to the Fe1 site in positions trans to the N32 pyridine nitrogen and N1 tertiary amine, respectively, whereas the O20 oxygen atom is in a trans position to the O1 atom from the μ-phenoxo bridge. Complex **2** has the same coordination environment around M^{III} and M^{II} as complex **1**. Both complexes show clearly the *facial* coordination of the tridentate pendant arms of the $BPBPMP^{2-}$ ligand around both metal centers. This arrangement is identical to those observed in the $Mn^{III}Mn^{II}$,[35] $Fe^{III}M^{II}$ (where M^{II} is Mn, Fe, Ni, Cu, and Zn),[36−40] and $Ga^{III}Zn^{II}$[29] di-μ-acetate complexes with the same ligand.

The bond lengths around the Fe1 center (av. 2.045 Å) in **1** are similar to those observed in the corresponding $Fe^{III}Mn^{II}$ (av. 2.049 Å),[37] $Fe^{III}Cu^{II}$ (av. 2.055 Å),[39] $Fe^{III}Zn^{II}$ (av. 2.048 Å),[33] and $Fe^{III}Ni^{II}$ (av. 2.045 Å) complexes.[26,38] The bond lengths around the Ga1 ion in **2** are slightly smaller (av. 2.013 Å) than those found around the Fe^{III} centers in the corresponding iron complexes, which is in full agreement with their atomic radius (0.62 vs 0.65 Å, respectively) and comparable with the Ga−N/O distances in the $Ga^{III}Zn^{II}$ complex (2.016 Å).[29] Therefore, the Ga^{III} ion can be considered a good and useful analogue of the Fe^{III} metal center in metalloenzymes and biomimetics.[28,29,32] On the other hand, a comparison of the average bond lengths around the Co1 centers in **1** (av. 2.115 Å) and **2** (av. 2.097 Å) is in agreement with other $M^{III}M^{II}$ complexes according to their atomic radii.[29,35−40] The terminal M^{III}−O-(phenolate) bond distances in **1** (1.888 Å) and **2** (1.906 Å) are similar to that found in the FeMn spPAP (1.88 Å)[21,54] and are within the range of bond lengths found in homo- and heterodinuclear complexes with the same ligand but are approximately 0.15 Å shorter than the $Fe^{III}-O_{tyr}$ found in the $Fe^{III}Zn^{II}$ rkbPAP enzyme (2.05 Å).[8] The $M^{III}\cdots Co^{II}$ distances found in **1** (3.489 Å) and **2** (3.484 Å) are longer but still comparable to the corresponding distances in rkbPAP[8] (3.26 Å) and Uf[13] (3.31 Å). The slight difference is most probably due to the presence of the di-μ-acetate bridge in **1** and **2**, whereas in the enzymes, the Fe^{III} and M^{II} ions are linked via a μ-hydroxo bridge. It is important to note that, in the $Fe^{III}(\mu$-OH)Zn^{II} complex with the same ligand, the $Fe^{III}\cdots Zn^{II}$ distance is 3.05 Å.[32] The Fe1−O1−Co1 angle (117.24°) in **1** is similar to the corresponding angle observed in complex **2** (119.67°) and also comparable to other isostructural di-μ-acetate heterodimetallic compounds with the same ligand.[29,26,34−40] However, these angles are significantly larger, as expected, when compared to the corresponding angle found in the $Fe^{III}(\mu$-OH)Zn^{II} complex (96.2°).[32]

Magnetochemistry. The magnetic data for complex **1** were obtained as a function of both the temperature and magnetic field. The variable-temperature data were collected in the temperature range 2.0−300 K at a constant magnetic field (0.1 T). The variable magnetic field data were collected in the field range 0−5 T at a temperature of 2 K. The experimental temperature dependence of χT is shown in Figure 4, and the magnetization versus field

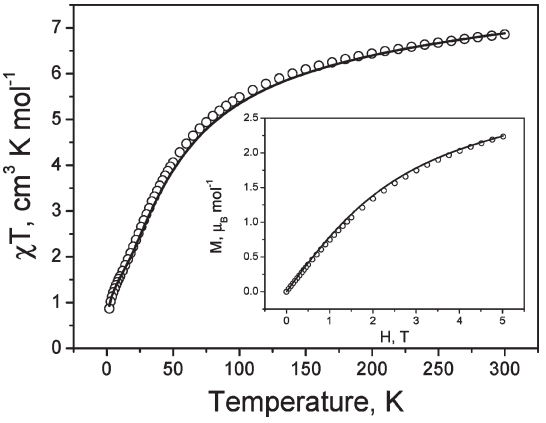

Figure 4. χT vs T for complex **1** measured at 0.1 T. The solid line represents the best fit calculated at $J = -5.0$ cm^{-1}, $\Delta = 916$ cm^{-1}, $\kappa = 0.7$, TIP $= 1.5 \times 10^{-3}$ cm^3 mol^{-1}. Inset: Magnetization vs field for complex **1** measured at 2 K. The solid line represents the best fit calculated at $J = -5.0$ cm^{-1}, $\Delta = 916$ cm^{-1}, $\kappa = 0.7$, TIP $= 1.5 \times 10^{-3}$ cm^3 mol^{-1}.

dependence $M(H)$ (in μ_B per formula unit) is shown in Figure 4 (inset). These results indicate the presence of antiferromagnetic exchange interactions between the Fe^{III} and Co^{II} centers.

Quantitative analysis of the data proceeds as follows. The Hamiltonian of complex **1** can be written as

$$\check{H} = \check{H}_{ex} + \check{H}_{SO} + \check{H}_{CF} + \check{H}_{Ze} \quad (3)$$

The first term in the total Hamiltonian, $\check{H}_{ex}$, represents the magnetic exchange between Co^{II} and Fe^{III} ions. Since the ground state of Co^{II} is orbitally degenerate ($^4T_{1g}$ triplet in a cubic crystal field, arising from the ^4F free-ion term, with contribution from the ^4P free-ion term), the exchange interaction should contain, in general, both orbital and spin contributions. However, following the idea of Lines,[55a] we assume that the exchange interaction between cobalt and iron centers contains only an isotropic part operating with the real spins and can be written as

$$\check{H}_{ex} = -2J\mathbf{S}_1\mathbf{S}_2 \quad (4)$$

where J is the exchange coupling parameter and $S_1 = 3/2$ and $S_2 = 5/2$ refer to the Co^{II} and Fe^{III} ions, respectively. The second term in the total Hamiltonian, $\check{H}_{SO}$, represents spin−orbit coupling in the Co^{II} ion. Focusing on the $^4T_{1g}$ ground state only (corresponding to the assumption that the ligand field is strong enough), we can describe Co^{II} as an ion with the fictitious angular momentum $L_1' = 1$. The spin−orbit interaction within the $^4T_{1g}$ triplet can be written as follows:

$$\check{H}_{SO} = -\frac{3}{2}\kappa\lambda\mathbf{S}_1\mathbf{L}_1 \quad (5)$$

where κ is the orbital reduction factor and λ is the spin−orbit coupling parameter for a free Co^{II} ion, which is most recently reported as $\lambda = -178$ cm^{-1}.[55b] The factor −3/2

(54) Schenk, G.; Gahan, L. R.; Carrington, L. E.; Valizadeh, M.; Hamilton, S. E.; de Jersey, J.; Guddat, L. W. *PNAS* **2004**, *102*, 273.

(55) (a) Lines, M. E. *J. Chem. Phys.* **1971**, *55*, 2977. (b) Bendix, J.; Brorson, M.; Schäffer, C. E. *Inorg. Chem.* **1993**, *32*, 2838. (c) Ostrovsky, S. M.; Falk, K.; Pelikan, J.; Brown, D. A.; Tomkowicz, Z.; Haase, W. *Inorg. Chem.* **2006**, *45*, 688. (d) Tomkowicz, Z.; Ostrovsky, S.; Müller-Bunz, H.; Hussein Eltmimi, A. J.; Rams, M.; Brown, D. A.; Haase, W. *Inorg. Chem.* **2008**, *47*, 6956.

appears because the matrix elements of L_1' within the $^4T_{1g}$ states are exactly the same as the matrix elements within an authentic P ($L = 1$) basis set multiplied by this factor. The orbital reduction factor κ takes into account not only the covalence of the cobalt−ligand bonds but also the combination of both $^4T_{1g}$ states (originating from ^4F and ^4P). Neglecting the covalence, we find that κ varies between 1 (weak-field limit) and 2/3 (strong-field limit).

The next term, $\check{H}_{CF}$, in eq 3 is the low-symmetry (noncubic) crystal-field term that takes into account distortion of the local surroundings of the Co^{II} ion (the cubic crystal field is accounted for above in $\check{H}_{SO}$). Combined with the spin−orbit interaction, this low-symmetry field gives rise to a strong magnetic anisotropy of the Co^{II} ion. Along the principal axes, the low-symmetry crystal field term can be written as

$$\check{H}_{CF} = \Delta\left[\hat{L}_{1z}^2 - \frac{1}{3}L_1(L_1+1)\right] + E(\hat{L}_{1x}^2 - \hat{L}_{1y}^2) \quad (6)$$

where Δ and E are the axial and rhombic splitting parameters, respectively. There is a correspondence between the sign of the Δ and the type of distortion. The ground state of a high-spin Co^{II} ion in an octahedral environment represents a superposition of two $^4T_{1g}$ states, namely, $|t_{2g}^5(^2T_{2g})e_g^2(^3A_2),^4T_{1g}\rangle$, arising from free-ion ^4F and $|t_{2g}^4(^3T_{1g})e_g^3(^2E_2),^4T_{1g}\rangle$, arising from free-ion ^4P. The coefficients in this superposition depend on the strength of the crystal field relative to interelectronic repulsion; however, the contribution of the $t_{2g}^5e_g^2$ configuration is always greater. It can therefore be assumed that the behavior of the high-spin Co^{II} ion in lower symmetry is largely determined by the behavior of this electronic configuration. The axial distortion along the local z axis leads to the splitting of e_g and t_{2g} states. A compression leads to stabilization of the d_{xy} orbital, whereas for elongation, d_{xz} and d_{yz} have the lowest energy. For the $t_{2g}^5e_g^2$ configuration, compression results in a doubly degenerate orbital ground state, whereas for elongation, there is no orbital degeneracy. In terms of eq 6, these distortions translate into negative and positive values of Δ, respectively, for compression and for elongation.

The last part, $\check{H}_{Ze}$, of the total Hamiltonian is the Zeeman interaction. For the high-spin Co^{II} ion, this consists of both spin and orbital contributions, and for the studied dinuclear complex it can be written as

$$\check{H}_{Ze} = \mu_B\left(g_{Co}\mathbf{S}_1 - \frac{3}{2}\kappa\mathbf{L}_1\right)\mathbf{H} + \mu_B g_{Fe}\mathbf{S}_2\mathbf{H} \quad (7)$$

where μ_B is the Bohr magneton, and g_{Co} and g_{Fe} are g factors for Co and Fe ions, respectively. If the spin−orbit interaction between the $^4T_{1g}$ ground state of Co^{II} and any excited states is neglected, g_{Co} is equal to the free electron value, $g_e = 2.0023$. After accounting for this interaction, g_{Co} is about 2.1.[55c] As for the Fe^{III} ion ($^6A_{1g}$ ground state), to reduce the number of fitting parameters, we neglect the difference between g_{Fe} and g_e, which is confirmed by EPR measurements (vide infra).

We start the analysis of the magnetic behavior by consideration of the local surroundings of the Co^{II} ion. It is difficult to find the type of distortion in the case of mixed-ligand surroundings. One possibility to solve this problem is the use of the crystal-field gradient tensor. The calculation details can be found elsewhere.[55d] The crystal electric field gradient tensor was diagonalized for the various relations of the nitrogen to oxygen charge (in the limits from 1 to 0.7). It was found that, in all cases, the distortion of the local surrounding of the Co^{II} ion can be described as an axial elongation of the local octahedron, with the rhombic distortion being small enough to be disregarded. Thus, the axial model ($E = 0$ in eq 6) for a Co^{II} ion with a positive value for Δ is a reasonable choice for the analysis of the magnetic behavior of **1**. Figure 4 shows calculated susceptibility and magnetization curves, respectively, generated using the best fit parameters given in the figure captions. One finds a good agreement between experimental data and theory, allowing extraction of the magnetic exchange coupling between the two ions.

In general, it has been observed that, for related complexes containing the mixed-valence $[Fe^{III}(\mu\text{-phenoxo})(\mu\text{-OAc})_2M^{II}]$ (M^{II} = Fe, Ni, Mn)[29,34,37,38] core with the unsymmetrical H_2BPBPMP[37] ligand, the antiferromagnetic interaction is weak and is in the range of −6.0 to −14 cm^{-1}. The antiferromagnetic coupling constant of −5.0 cm^{-1} obtained for the isostructural $Fe^{III}Co^{II}$ complex here presented lies in the lower end of the range of values found for these $[Fe^{III}(\mu\text{-phenoxo})(\mu\text{-OAc})_2M^{II}]$ complexes. In addition, it has been found that, within the series of three complexes with the H_2BPBPMP ligand, $[Fe^{III}(\mu\text{-phenoxo})(\mu\text{-OAc})_2Ni^{II}]$,[29,38] $[Fe^{III}(\mu\text{-phenoxo})(\mu\text{-OAc})Ni^{II}]$,[26] and $[Fe^{III}(\mu\text{-phenoxo})Ni^{II}]$,[26] there are significantly distinct Fe−O−Ni angles (118.66°, 119.17°, and 124.20°, respectively) but similar $Fe^{III}-(\mu\text{-}O_{phenoxo})$ and $Ni^{II}-(\mu\text{-}O_{phenoxo})$ distances, and the exchange coupling constants are of similar magnitude (∼−13.5 cm^{-1}). Indeed the magnitude of the parameter J determined for all of these $Fe^{III}Ni^{II}$ complexes allows us to conclude that the major pathway for exchange coupling is mediated via the phenoxo bridge and that the acetate groups and the $Fe^{III}-O-Ni^{II}$ angle have very little effect on the magnetic properties of the dinuclear center.[26]

Given the availability of accurate X-ray structural data and magnetic exchange parameters for this series of heterodinuclear $Fe^{III}M^{II}$ complexes in which only the M^{II} center has been changed, it is important to identify and evaluate the structural and electronic factors that influence the exchange coupling constant. Werner et al.[56a] have established a reformulated empirical magneto-structural correlation, originally published by Gorun and Lippard,[56b] in this case for homodinuclear di- and tribridged $[Fe^{III}(\mu\text{-X})(\mu\text{-Y})Fe^{III}]$ complexes (X = hydroxo, phenoxo, and alkoxo and Y = acetate, arsenate, cromate, and phosphate) in which the mean iron−oxygen distance d of the $Fe^{III}-O-Fe^{III}$ bridge is the most important structural factor in determining the magnitude of the exchange coupling.[56a] The empirical relationship has been quantified in the form $J = -10^7\exp(-6.8d)$. Interestingly, an estimation of the exchange interaction in the mixed-valence $[Fe^{III}(\mu\text{-phenoxo})(\mu\text{-OAc})_2M^{II}]$ (M^{II} = Mn, Fe, Co, Ni) complexes using this relationship and d

(56) (a) Werner, R.; Ostrovsky, S.; Griesar, K.; Haase, W. *Inorg. Chim. Acta* **2001**, *326*, 78. (b) Lippard, S. J.; Gorun, S. M. *Inorg. Chem.* **1991**, *30*, 1625. (c) Weihe, H.; Güdel, H. U. *J. Am. Chem. Soc.* **1997**, *109*, 6539.

Table 3. Structural Parameters and Magnetic Data for the [Fe^{III}(μ-phenoxo)(μ-OAc)$_2M^{II}$] Complexes

complex	$Fe^{III}-O_{ph}$ (Å)	$M^{II}-O_{ph}$ (Å)	d (Å)[a]	α (^{deg})[b]	J_{exp} (cm^{-1})	J_{calcd} (cm^{-1})[c]	ref
$Fe^{III}Mn^{II}$	2.010	2.155	2.082	114.86	−6.8	−7.1	37
$Fe^{III}Fe^{II}$	2.005	2.102	2.053	117.14	−7.4	−8.6	34
$Fe^{III}Co^{II}$	2.014	2.073	2.043	117.24	−5.0	−9.2	this study
$Fe^{III}Ni^{II}$	1.995	2.058	2.026	118.66	−13.3	−10.3	26, 38

[a] Average distance between $Fe-O_{ph}$ and $M^{II}-O_{ph}$. [b] Bridging angle of the $Fe^{III}-O-M^{II}$ unit. [c] Calculated by $J = -10^7 \exp(-6.8d)$.

as the average bond lengh of the [$Fe^{III}-O-M^{II}$] structural unit reveals that the calculated data are in good agreement with the J (cm^{-1}) values determined from magnetic measurements (Table 3). In fact, as can be observed in Table 3, within the series of [Fe^{III}(μ-phenoxo)(μ-OAc)$_2M^{II}$] complexes studied, the shorter the $Fe^{III}-(\mu\text{-}O_{ph})$ and the $M^{II}-(\mu\text{-}O_{ph})$ bond distances, the stronger the exchange coupling, an observation which is in full agreement with Werner's relationship employed in the present calculations, with the exception of the $Fe^{III}Co^{II}$ system.

From this information, it seems reasonable to conclude that the antiferromagnetic contribution is decisively influenced by the overlap integral S of the participating natural Fe^{III} and M^{II} magnetic orbitals and that the absolute value of S increases with the shortening of the $Fe^{III}-O_{ph}$ and $M^{II}-O_{ph}$ distances. Apparently, as has been observed for the homodinuclear [Fe^{III}(μ-X)Fe^{III}] complexes (X = hydroxo, phenoxo, alkoxo), the resulting exchange interaction for the complexes presented here also does not exhibit an $Fe^{III}-O_{ph}-M^{II}$ angle dependency. Even for the $Fe^{III}Mn^{II}$ complex, which has the smallest $Fe^{III}-O_{ph}-M^{II}$ angle within this series of compounds, the $J = -7.1$ cm^{-1} calculated according to the equation $J = -10^7 \exp(-6.8d)$ is in excellent agreement with the value obtained from magnetic measurements ($J = -6.8$ cm^{-1}). In addition, the fact that the J values obtained for the $Fe^{III}M^{II}$ systems using the semiempirical equation developed by Weihe and Güdel[56c] for dinuclear Fe^{III}(μ-O)Fe^{III} complexes (the $Fe^{III}-O-Fe^{III}$ angle is also taken into account) are about 3 times higher when compared to the values determined experimentally strongly corroborates this conclusion. Nevertheless, it should be emphasized that the large number of superexchange pathways makes a detailed qualitative analysis of such systems very difficult since the number of participating magnetic orbitals at the M^{II} center changes from five (Mn^{II}) to two (Ni^{II}), while the spherical Fe^{III} high-spin (d^5) ion remains unchanged. Deviation between the calculated and experimental J values (−9.2 and −5.0 cm^{-1}, respectively) for the $Fe^{III}Co^{II}$ system within this [Fe^{III}(μ-phenoxo)(μ-OAc)$_2M^{II}$] series of complexes is strong evidence of the difficulty in interpreting the electronic or structural factors that can affect the exchange coupling between the Fe^{III} and M^{II} centers in these mixed-valence complexes.

Finally, a structural comparison with other $Fe^{III}Co^{II}$ systems is not possible since there are no such systems described in the literature, even for the $Fe^{III}Co^{II}$ PAP derivative, for which only spectroscopic and kinetic properties have been reported.[20−23]

HFEPR Spectroscopy. Complexes **1**, **2**, and **3** were investigated by high-frequency and -field electron paramagnetic resonance (HFEPR) spectroscopy as undiluted solid powders. This technique can provide information that is both complementary and supplementary to that provided by magnetometric measurements such as those described in the previous section.[45] The antiferromagnetic interaction between the Fe^{III} and Co^{II} ions in **1** indicates that the ground spin state can be described as $S_T = S_1 - S_2 = 1$. The relatively small value of J makes it possible to thermally populate a variety of excited states, up to $S_T = S_1 + S_2 = 4$. Such a high-spin system could in principle yield a large number of magnetic dipole-allowed EPR transitions. For example, HFEPR of an Fe dimer with an $S_T = 9/2$ ground state (resulting from ferromagnetically coupled high-spin Fe^{II} and Fe^{III} ions) was successfully determined to yield the spin-Hamiltonian parameters of the coupled system.[57] However, HFEPR spectroscopy of such systems is not always fruitful, as some of us have experienced severe difficulties with integer S_T exchange-coupled tetranuclear complexes.[58] We can only speculate that fast relaxation and strain effects have affected HFEPR spectra in those cases.

In the case of **1**, an intermediate situation resulted. Complex **1** did not produce rich HFEPR spectra, even at elevated temperatures. However, **1** was not totally "silent" either; it did show well-defined responses in a 92−280 GHz frequency region, and at low temperatures (5−10 K). Figure 5 (inset) shows a pair of resonances observed very near zero field in the 92−112 GHz frequency range and at $T = 10$ K. With increasing frequency, the signals move to higher fields and gradually merge into a single, broad line, observable up to 280 GHz. Other than two weak signals, one appearing at $g = 2.00$ and the other at $g = 2.10$ at any frequency (not shown), which we attribute to trace impurities, no more resonances were observed in **1**.

Figure 5 (main figure) shows the 2-D field/frequency map of the EPR resonances observed in **1**. This map can be potentially interpreted as originating from an $S = 1$ spin state. In particular, the two resonances observed at the lowest frequency limit originate in this picture from the zero field $|D - E|$ and $|D + E|$ transitions characteristic for the triplet state. Their frequency behavior is also characteristic, particularly in the way the two signals merge at higher frequencies and fields into a single peak, known in the EPR spectroscopy of the triplet state as B_{min}, which represents the nominally forbidden $\Delta M_S = \pm 2$ transition. B_{min} is typically the strongest peak in a triplet powder spectrum, which explains why, given a modest signal-to-noise ratio, no other resonances were observed for **1**. The set of spin-Hamiltonian parameters

(57) Knapp, M. J.; Krzystek, J.; Brunel, L.-C.; Hendrickson, D. N. *Inorg. Chem.* **1999**, *38*, 3321.
(58) Karadas, F.; Schelter, E. J.; Shatruk, M.; Prosvirin, A. V.; Bacsa, J.; Smirnov, D.; Ozarowski, A.; Krzystek, J.; Telser, J.; Dunbar, K. R. *Inorg. Chem.* **2008**, *47*, 2074.

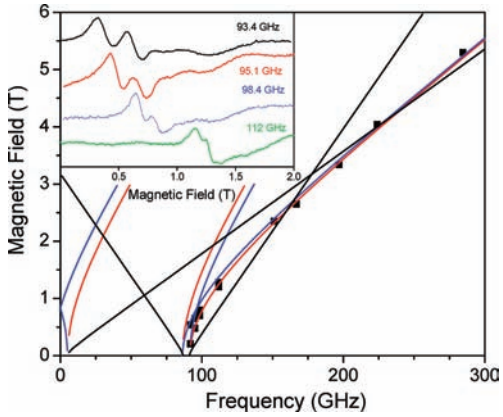

Figure 5. (Inset) EPR spectra of complex **1** near the double zero-field transition at $T = 10$ K and indicated frequency using a conventional (magnetic) modulation resulting in a derivative shape. (Main plot) 2-D field/frequency map of EPR transitions in the same complex. The squares are experimental points, while the lines were calculated using the following spin-Hamiltonian parameter set: $S = 1$, $|D| = 2.97$ cm^{-1}, $|E| = 0.09$ cm^{-1}, $g_x = g_y = 1.85$, $g_z = 2.00$. The red lines denote the turning points with $B_0 \| x$; the blue lines, those with $B_0 \| y$; and the black lines, those with $B_0 \| z$.

that best fits the field/frequency map with $S = 1$ is $|D| = 2.97(1)$, $|E| = 0.09(1)$ cm^{-1}, $g_{x,y} = 1.85(5)$, and $g_z = 2.00$, with the g_z value assumed. This fit value for $g_{x,y}$ is surprisingly low, given that the single-ion g values, g_{Co} and g_{Fe}, are ≥ 2.0, and likely reflects the oversimplification of treating **1** as a simple $S = 1$ system. Ideally, the HFEPR data should be simulated using a model that explicitly treats both of the constituent ions of **1**, including the orbital contribution to the Co^{II} component and the exchange coupling between this ion and Fe^{III}. However, such an analysis is beyond the scope of this study, which simply demonstrates that **1** exhibits EPR behavior consistent with an antiferromagnetically coupled Fe^{III}-Co^{II} species.

HFEPR was more profitably applied to the two analogs of **1** in which each paramagnetic metal ion had been replaced by a diamagnetic one, namely, **2** (Ga^{III} for Fe^{III}) and **3** (Zn^{II} for Co^{II}). As described above, the Co^{II} ion in octahedral symmetry experiences a very large orbital angular momentum contribution, which leads to EPR behavior quite unlike that for simple radicals: an isotropic g value far from g_e is observed; ideally, $g_{Co}' = 4.33$[46] (the prime indicates that this is an *effective g* value, not the intrinsic g_{Co} value given in the Magnetochemistry section). However, axial distortion, whether trigonal or tetragonal, can lead to significant anisotropy in the observed g values. For example, even in a complex with homoleptic O_6 coordination, $[Co(py\text{-}O)_6](ClO_4)_2$ (py-O = pyridine *N*-oxide), $g_\perp' = 4.70(5)$ and $g_\| ' = 2.49(5)$.[59] Makinen et al. have summarized experimental data for many other representative systems.[60]

HFEPR studies of **2** produced high-quality powder-patterned spectra characteristic for HS Co(II) with a strong rhombic anisotropy (see Figure 6 inset). By fitting the effective $S' = 1/2$ spin-Hamiltonian parameters to the 2-D frequency/field map of the observed turning points

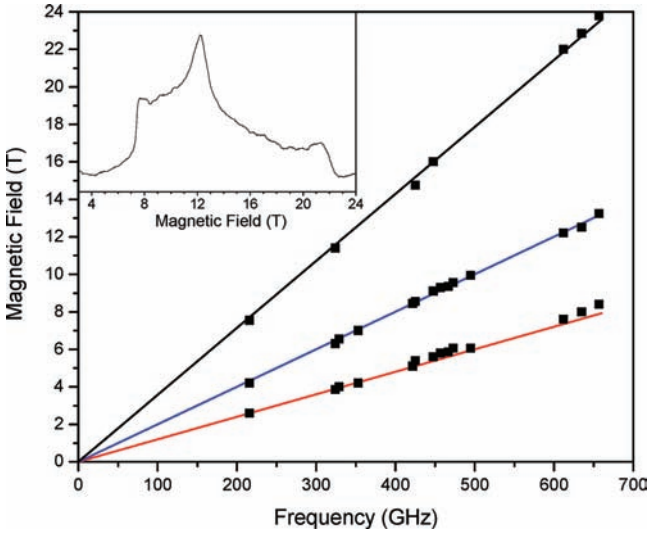

Figure 6. (Inset) A 635 GHz EPR spectrum of complex **2** at 4.2 K recorded using optical modulation (chopping) of the submillimeter wave beam, resulting in an absorptive shape. (Main plot) 2-D field/frequency map of HFEPR turning points in the spectra of **2** at 4.2 K. The squares are experimental points, while the lines were generated using the best-fitted effective spin-Hamiltonian parameters: $S' = 1/2$, $g_x' = 5.75$, $g_y' = 3.60$, $g_z' = 2.00$. The red line denotes the turning points with $B_0 \| x$; the blue line, those with $B_0 \| y$; and the black line, those with $B_0 \| z$.

(Figure 6, main figure), we obtained the following values: $g_x' = 5.75(5)$, $g_y' = 3.60(2)$, and $g_z' = 2.00(1)$. This rough ordering of g values ($g_\perp' \gg g_\| ' \geq g_e$) results from an orbitally nondegenerate ground state (due to axial elongation, $\Delta > 0$), which is in agreement with the results of the magnetic analysis (the opposite ordering of g values would result from axial compression and an orbitally degenerate ground state). If one ignores the rhombic anisotropy, then the value for $g_\perp' = 4.675$, which is very close to that reported for $[Co(py\text{-}O)_6](ClO_4)_2$.[59] This electronic rhombic distortion is also suggested structurally, namely, by the three sets of Co−(O/N) bond lengths of **2** in the solid state: two bond lengths of ~2.042(10) Å, two at 2.098(3) Å, and two at 2.166(4) Å (see Table 2).

If sufficiently high frequencies were available, then it would be possible in principle to observe EPR transitions from the spin−orbit ground state to states of higher spin−orbit multiplicity and derive from magnetic resonance spectroscopy the magnitude of Δ, which was estimated by the magnetic measurements. In an octahedral Co^{II} system, the lowest of these excited states (in zero applied field) would appear at energies as much as hundreds of centimeters^{-1} above the ground state. Efforts to observe these transitions should become possible through the use of terahertz sources, which is a current research direction in HFEPR spectroscopy.

In addition to HFEPR, a frozen-solution 35 GHz ("Q"-band) spectrum was recorded for **2** at 2 K (Figure S1, Supporting Information). To correspond to the electronic absorption studies (see below), acetonitrile was used, but not as a neat solvent. A 1:1 v/v acetonitrile/toluene was used; toluene cosolvent is needed to provide glassing properties, while being noncoordinating to the metal complex. This single-frequency spectrum provided $g_{3(max)}' = 5.80(1)$, $g_{2(mid)}' = 3.95(5)$, and $g_{1(min)}' = 2.09(1)$, where the average between g_3' and g_2' corresponds to $g_\perp' \approx 4.88$ (again similar to the value found for the

(59) Carlin, R. L.; O'Connor, C. J.; Bhatia, S. N. *J. Am. Chem. Soc.* **1976**, *98*, 685.
(60) Makinen, M. W.; Kuo, L. C.; Yim, M. B.; Wells, G. B.; Fukuyama, J. M.; Kim, J. E. *J. Am. Chem. Soc.* **1985**, *107*, 5245.

hexakis(py-O) complex[59]), and g_1' is equivalent to $g_{\|}'$ (g_z'). These frozen-solution g' values are very close to those determined for solid state **2** by multiple, high frequencies: $g_x' = 5.75(5)$, $g_y' = 3.60(2)$, and $g_z' = 2.00(1)$. Thus, the electronic structure of the Co^{II} ion in **2** is consistent between frozen solution and the solid state. No hyperfine coupling from ^{59}Co (100%, $I = 7/2$) was resolved, as the lines were very broad and anisotropic ($W_1 = 1.8$, $W_2 = 3.0$, and $W_3 = 1.0$ GHz, Gaussian half-width at half-maximum).

The $Fe^{III}Zn^{II}$ complex, **3**, was also investigated by HFEPR as a solid powder. High-spin Fe^{III} can be studied by conventional (e.g., X-band) EPR; however, unless the environment is strongly axial (e.g., in porphyrinic complexes), the spectra are often dominated by the so-called "junk iron" signal at $g' \approx 4.3$. Careful analysis, however, does allow extraction of useful parameters from X-band spectra, as convincingly shown in the recent study by Weisser et al.[61] on Fe^{III}tris(catecholate) complexes, and by Renault et al.[62] on FeSOD (superoxide dismutase). HEFPR studies on Fe^{III} are reviewed by Krzystek et al.[45a] The utility of HFEPR in the study of such systems was recently demonstrated by Biaso et al. for Fe^{III}(citrate) complexes.[63] This paper also provides an excellent summary of EPR parameters for high-spin Fe^{III}.[63] In the case of **3**, we have used HFEPR to extract the full set of spin-Hamiltonian parameters for the Fe^{III} ion. A typical spectrum, in this case at 216 GHz and 10 K, is shown in Figure 7 together with its simulation using the following spin-Hamiltonian parameters: $S = 5/2$, $D = +0.41$ cm^{-1}, $|E| = 0.098$ cm^{-1}, $g_x = 1.96$, $g_y = 2.00$, $g_z = 2.02$. The pronounced rhombicity of the ZFS tensor ($E/D = 0.24$, with 0.33 being the maximum value possible) should be noted; an axial ZFS tensor could not reproduce the observed intensities of particular ΔM_S transitions. The HFEPR results for **3** confirm that g_{Fe} is essentially 2.00 ± 0.05, as assumed above in the Magnetochemistry section. The magnitude of the ZFS is on the same order of magnitude as in $[Fe^{III}(EDTA)(H_2O)]^-$, for which $|D| = 0.84$ cm^{-1}.[64] This EDTA complex comprises ligands that resemble those of **3**, although their coordination geometry is different. The Fe^{III}tris(catecholate) complexes have been estimated to have a D of magnitude $\sim 0.4(2)$ cm^{-1},[61] which is even closer to the value observed by us in **3**, while the citrate complex has a much lower magnitude of D (0.024 cm^{-1} at pH 6.2).[63] The ZFS in high-spin d^5 complexes (e.g., Mn^{II} and nonporphyrinic/heme Fe^{III}) is generally moderate ($|D| < 1$ cm^{-1}), resulting from many types of (often counteracting) spin−orbit and spin−spin contributions, and has challenged even the leading computational chemists.[65−67] Thus, simple attempts at quantitative comparisons should be regarded with great skepticism. In principle, the single-ion ZFS of the Fe^{III} site should be included in the magnetic analysis; however, as shown by the HFEPR data, this contribution is sufficiently small to be ignored, so that spin−orbit effects only on the Co^{II} site need be considered, as described above. A general consequence of this HFEPR study of **3**, and the recent work of Biaso et al.,[63] is that this technique can be readily applied to determine ZFS in highly rhombic high-spin Fe^{III} systems, which could lead to a wider application in bioinorganic chemistry, specifically to nonheme Fe enzymes, such as in FeSOD.

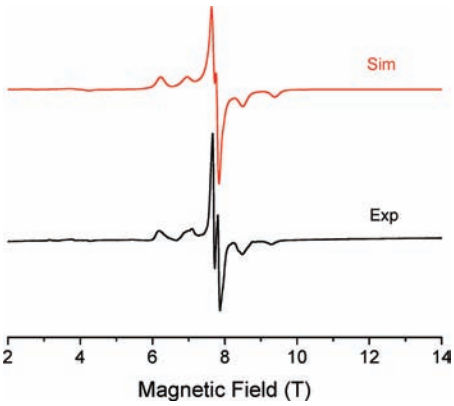

Figure 7. A 216 GHz EPR spectrum of polycrystalline complex **3** recorded at 10 K using a conventional (magnetic) modulation, resulting in a derivative shape. The black trace is the experimental, while the red trace is a simulation assuming a perfect powder pattern and using spin-Hamiltonian parameters as in the text.

MCD Spectroscopy. To complement and connect the magnetometric measurements (vide supra) and electronic absorption spectroscopic studies (vide infra), MCD spectra were recorded for **1** and **2** as mull samples. All spectra obtained for **1** and **2** show a decrease in intensity with increasing temperature, which means that all bands arise from temperature-dependent C terms. Given that complex **2** has only one paramagnetic ion, Co^{II}, this complex was analyzed first. The MCD spectrum of **2** is shown in Figure 8, which also displays the resolution of the spectrum into the minimum number of Gaussian components over the wavelength region 250−500 nm.

The MCD spectrum of **2** could be well-fitted with six Gaussian components. The bands obtained are centered at 260, 278, 299, 338, 374, and 455 nm. The first negative

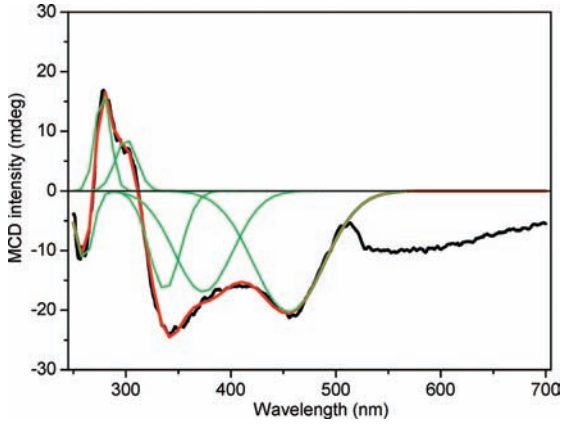

Figure 8. MCD spectrum of **2** recorded at 5 K and a field of 8 T. The Gaussian components are shown as thin green lines, and the thick red line is a fit in the wavelength region 250−500 nm.

(61) Weisser, J. T.; Nilges, M. J.; Sever, M. J.; Wilker, J. J. *Inorg. Chem.* **2006**, *45*, 7736.
(62) Renault, J. P.; Verchere-Beaur, C.; Morgenstern-Badarau, I.; Yamakura, F.; Gerloch, M. *Inorg. Chem.* **2000**, *39*, 2666.
(63) Biaso, F.; Duboc, C.; Barbara, B.; Serratrice, G.; Thomas, F.; Béguin, C. *Eur. J. Inorg. Chem.* **2005**, 467.
(64) Aasa, R. *J. Chem. Phys.* **1970**, *52*, 3919.
(65) Zein, S.; Duboc, C.; Lubitz, W.; Neese, F. *Inorg. Chem.* **2008**, *47*, 134.
(66) Zein, S.; Neese, F. *J. Phys. Chem. A* **2008**, *112*, 7976.
(67) Duboc, C.; Phoeung, T.; Zein, S.; Pécaut, J.; Collomb, M.-N.; Neese, F. *Inorg. Chem.* **2007**, *46*, 4905.

and positive bands may be so-called pseudo-A terms. The band at 455 nm can be assigned to the $^4T_1(F) \rightarrow {}^4T_1(P)$ d−d transition, which is usually observed near 500 nm. This band broadens when $^4T_1$ terms split under lower symmetry. We note that the spectrum of **2** is not typical for Co^{II} in octahedral coordination. Johansson et al.[68] reported MCD spectra for a weakly exchange-coupled $Co^{II}Co^{II}$ dimer and for a paramagnetic $Co^{II}Co^{III}$ dimer (Co^{III} is diamagnetic and thus analogous to Ga^{III}). These dimers have similarly distorted octahedral coordination for both ions, with O_3N_3 donor sets: one amine N donor, two pyridine N donors, one phenolate O, and two O donors from the diphenylphosphate group; the coordination sphere about Co^{III} is contracted. These coordination spheres are thus similar to the O_3N_3 coordination spheres of Co^{II} in **1** and **2**, only instead of diphenylphosphate there are two acetates. However, the MCD spectra of the $Co^{II}Co^{III}$ dimer and of **2** are strikingly different. Johansson et al. differentiate only one d−d transition at ∼500 nm in the spectral region 300−700 nm. The other resolved components are tentatively attributed to ligand-to-metal charge-transfer transitions (LMCT); in particular, two transitions are expected from phenolate oxygen to Co^{II} LMCT.

MCD magnetization curves for **2**, recorded at $\lambda = 460$ nm, are plotted as the function $\mu_B H/2kT$ in Figure S2 (Supporting Information). As is seen, the curves are strongly fanned out. This behavior could result from the superposition of a small d−d band near 500 nm with a charge-transfer transition of different polarization at a lower wavelength. In contrast, the $Co^{II}-Co^{III}$ dimer exhibits variable-temperature−variable-field MCD signals that overlap for different bands,[68] such behavior corresponding to a Kramers doublet, as expected at low symmetry and $\Delta > 0$. We do not know the value of Δ for complex **2**, but for **1**, the value of Δ is positive (vide supra).

In Figure 9, spectra obtained at 8 T and 5 K for both **1** and **2** are compared. Additionally, the spectra for **1** ($Fe^{III}Co^{II}$) are shown for various magnetic fields, and the spectrum obtained at a relatively high temperature of 90 K and 8 T is also shown. As is seen, the $Fe^{III}Co^{II}$ spectrum for 5 K is strongly modified with respect to the spectrum of **2** ($Ga^{III}Co^{II}$) by the presence of Fe^{III} and spin exchange between Fe^{III} and Co^{II}. Although the individual contribution of Fe^{III} is small, as all Fe^{III} d−d transitions are spin-forbidden, nonetheless a number of phenolate O to Fe^{III} transitions are expected.[69] In particular, the continuous part of the spectrum in the low-energy region may be due to charge-transfer transitions from phenolate. MCD magnetization curves were obtained for **1** at two wavelengths: 496 nm (shown in the Supporting Information, Figure S3, main figure) and 353 nm (Supporting Information, Figure S3, inset). Interestingly, that recorded at $\lambda = 496$ nm showed no fanning out; however, at $\lambda = 353$ nm, a large fanning out was observed. This complicated behavior needs more detailed computational analysis.

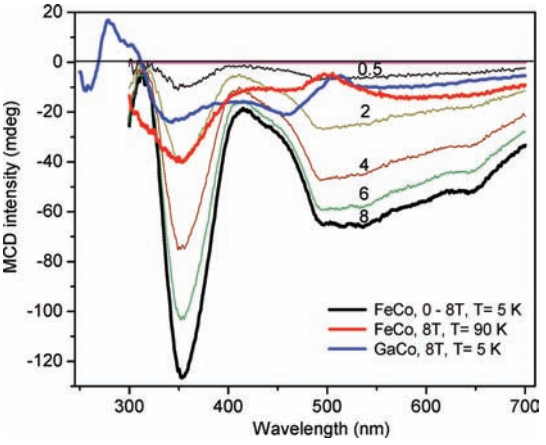

Figure 9. Comparison of the MCD spectra for **1** ($Fe^{III}Co^{II}$) and **2** ($Ga^{III}Co^{II}$). Complex **1** spectra are shown for two temperatures, 5 and 90 K, and the spectra for 5 K are shown for various magnetic fields from 0 up to 8 T. Three spectra for 8 T are differentiated with a thick line: $Fe^{III}Co^{II}$ for 5 K (solid black line), $Fe^{III}Co^{II}$ for 90 K (solid red line), $Ga^{III}Co^{II}$ for 5 K (solid blue line which starts from 250 nm). Because the thickness of the samples was not controlled, the intensity for the $Ga^{III}Co^{II}$ sample is not closely connected with the intensity of the $Fe^{III}Co^{II}$ spectrum.

Electronic Absorption Spectroscopy. Electronic spectra of **1** (Supporting Information, Figure S4, top) and **2** (Supporting Information, Figure S4, bottom) were recorded in acetonitrile (I), under kinetic conditions (II), and in the solid state (III). For **1**, the electronic spectrum in acetonitrile solution shows a broad band at 544 nm (ε = 3760 M^{-1} cm^{-1}), which can be attributed to the terminal phenolate-to-Fe^{III} charge-transfer transition. A shoulder at 322 nm is also observed, which most probably arises from a second phenolate-to-Fe^{III} charge-transfer transition.[33,37−40] Under kinetic conditions, the electronic spectrum of **1** shows a similar behavior (478 nm; ε = 2930 M^{-1} cm^{-1}), but a hypsochromic shift was observed. This result can be interpreted in terms of distinct coordination environments around the metal centers in the two solvent systems. Thus, in acetonitrile solution, it is assumed that the carboxylates remain bound to the metal centers within the $\{Fe^{III}(\mu\text{-}OAc)_2Co^{II}\}$ core. When **1** is dissolved in an aqueous solution, the two bridging carboxylates are removed and are likely replaced by water molecules to form a $\{Fe^{III}(\mu\text{-}OH)Co^{II}\}$ unit (vide infra). Terminal H_2O/OH^- molecules most probably complete the hexacoordination around the Fe^{III} and Co^{II} centers. The hypsochromic shift from 544 to 478 nm may be due to the increase in the electron donation when the acetate ligand is replaced by OH^-, thus lowering the Lewis acidity of the Fe^{III} center, so that the t_{2g} orbitals are at higher energy in the $[Fe^{III}(\mu\text{-}OH)Co^{II}]$ species. This interpretation is also in agreement with the electronic spectral data observed in the corresponding $Fe^{III}Zn^{II}$ acetate complex.[32] The diffuse reflectance spectrum (Supporting Information, Figure S4, top, spectrum III) reinforces the idea of the solvent influence on the ligand field where two bands (584 and 356 nm) are registered. In this case, a bathochromic shift can be observed in comparison to the spectrum of **1** in CH_3CN. In general, the electronic properties of **1** are consistent with other $[Fe^{III}M^{II}(BPBPMP)(\mu\text{-}OAc)_2]^+$ complexes[33,37−40] (where M^{II} can be Fe, Ni, Cu, and Zn). Furthermore, the

(68) Johansson, F. B.; Bond, A. D.; Nielsen, U. G.; Moubaraki, B. K.; Murray, S.; Berry, K. J.; Larrabee, J. A.; McKenzie, C. J. *Inorg. Chem.* **2008**, *47*, 5079.
(69) Davis, M. I.; Orville, A. M.; Neese, F.; Zaleski, J. M.; Lipscomb, J. D.; Solomon, E. I. *J. Am. Chem. Soc.* **2002**, *124*, 602.

chromophoric features of the $\{Fe^{III}(\mu\text{-OH})Co^{II}\}$ species can also be also compared with the modified $Fe^{III}Co^{II}$ derivative of rkbPAP that shows a tyrosine-to-Fe^{III} charge-transfer transition at 518 nm (ε =3370 M^{-1} cm^{-1}).[1] The diffuse reflectance spectrum of **1** can also be compared to its MCD spectra (Figure 9), which demonstrates the concordance of these techniques. The resolved band seen at 356 nm corresponds to the strong MCD band at 353 nm, and the very broad absorption band in the range 450−800 nm corresponds to the partially resolved features seen in MCD spectra in this region (Figure 9).

In the visible region, complex **2** shows only one band at 423 nm (ε = 391 M^{-1} cm^{-1}) in acetonitrile solution, which is assigned to a Co^{II} d−d electronic transition (the replacement of Fe^{III} by Ga^{III} eliminates the phenolate-to-M^{III} LMCT transitions). A shoulder can also be observed in spectra I and III (Supporting Information, Figure S4, bottom) attributed to a superposition of further Co^{II} d−d transitions. Under kinetic conditions (spectrum II), the absorption of the d−d transitions of **2** are negligible due to their low molar absorption coefficients. The diffuse reflectance spectrum of **2** is only slightly shifted to a higher wavelength (spectrum III) when compared to the spectrum obtained in CH_3CN (spectrum I), which suggests that the coordination of the bridging acetate groups remains unchanged when the complex is dissolved in acetonitrile. The resolved band at 448 nm in the diffuse reflectance spectrum (III) clearly corresponds to that observed at 455 nm in the MCD spectrum of solid state **2** (Figure 8), with MCD spectroscopy providing much better resolution of these features.

Electrochemical Measurements. The electrochemical properties of **1** and **2** were determined by cyclic voltammetry in acetonitrile (0.1 M *n*-Bu_4NPF_6 as supporting electrolyte). The cyclic voltammograms with scan-rate variation (Supporting Information, Figure S5, top) of **1** reveal a *quasi*-reversible cathodic wave (−0.97 V vs Fc/Fc^+) ascribed to the one-electron redox process $Fe^{III}Co^{II}/Fe^{II}Co^{II}$ and an irreversible anodic process (−0.16 V vs Fc/Fc^+) which is assigned to the $Fe^{III}Co^{III}/Fe^{III}Co^{II}$ redox pair. For complex **2**, cyclic voltammograms (Supporting Information, Figure S5, bottom) show a single anodic process (−0.10 V vs Fc/Fc^+) which is ascribed to the redox process $Ga^{III}Co^{III}/Ga^{III}Co^{II}$. The value for the Fe^{III}/Fe^{II} redox couple of **1** is in close agreement with the values observed for the isostructural $Fe^{III}Mn^{II}$ (−0.87 V),[37] $Fe^{III}Fe^{II}$ (−0.89 V),[40] $Fe^{III}Ni^{II}$ (−0.94 V),[38] $Fe^{III}Zn^{II}$ (−0.91 V),[33] and $Fe^{III}Cu^{II}$ (−1.0 V)[39] complexes. This electrochemical behavior implies that the N_2O_4 coordination environment around the Fe^{III} imposes a particular potential for the Fe^{III}/Fe^{II} redox couple (in CH_3CN solution), of −0.95(5) V (vs Fc/Fc^+). Likewise, the $E^{1/2}$ = −0.16 V ascribed to the Co^{III}/Co^{II} redox couple in **1** compares favorably to the single redox couple $E^{1/2}$ = −0.10 V observed for the corresponding $Ga^{III}Co^{II}$ complex (**2**). Thus, the N_3O_3 coordination sphere around the Co^{II} center in **1** and **2** leads to a roughly common value for the Co^{III}/Co^{II} redox couple of −0.13(3) V (vs Fc/Fc^+).

Potentiometric and Spectrophotometric Titrations. Potentiometric titrations of complexes **1** and **2** were carried out, in triplicate, in a mixture of CH_3CN/H_2O (50/50 v/v; I = 0.1 mol L^{-1} KCl) and show the neutralization of 3 mol of KOH per mol of complex in the pH range of 3−11. Fitting the data with the BEST7[47] program resulted in the pK_a values given in Table 4. The three-deprotonation/protonation equilibrium steps are proposed in Scheme 1. The corresponding species distribution is shown graphically in Figure S6 (Supporting Information).

Table 4. Potentiometric pK_a Values Found for Complexes **1** and **2** in CH_3CN/H_2O (50:50 v/v) Solution

complex	**1**	**2**
pK_{a1}	5.00 ± 0.10	5.46 ± 0.02
pK_{a2}	6.58 ± 0.10	6.57 ± 0.02
pK_{a3}	8.31 ± 0.10	8.30 ± 0.03

For both complexes, the protonation equilibria can be interpreted in terms of the dissociation of the bridging-carboxylate groups (Scheme 1). First, one acetate group is released, leading to the $[(H_2O)M^{III}(\mu\text{-OAc})Co^{II}(H_2O)]$ species (structure A in Scheme 1), where pK_{a1} corresponds to the M^{III}-bound aqua ligand deprotonation to yield the $[(HO)M^{III}(\mu\text{-OAc})Co^{II}(H_2O)]$ species (structure B in Scheme 1). It has been proposed that, upon the dissociation of the second acetate group, water molecules occupy the remaining coordination positions of the metal ions.[28,29] Upon the deprotonation of a second water molecule, a μ-OH bridge is formed (pK_{a2}), generating the catalytically active species $[(HO)M^{III}(\mu\text{-OH})Co^{II}(H_2O)]$ (structure C in Scheme 1; vide infra). In the last step of the equilibrium process, pK_{a3} is assigned to the deprotonation of the Co^{II}-bound H_2O ligand to yield structure D in Scheme 1. The similarity between the corresponding pK_a values for the two complexes (pK_{a3} of 8.3) strongly corroborates this assignment.

Spectrophotometric titration experiments with complex **1** under kinetic conditions (CH_3CN/H_2O, 50/50 v/v) reveal that the λ_{max} position of the LMCT process is strongly dependent on the pH of the solution. In the pH ranges 4.03−5.75, 5.96−7.79, and 7.50−9.73, strict isosbestic points can be observed, indicating the presence of only two species in equilibrium, during each individual spectral change. The pK_a values of 4.7, 7.0, and 8.0 obtained from the spectral change (Supporting Information,Figure S7) are consistent with the potentiometric data and the equilibria proposed in Scheme 1.

Indeed, the pK_a values obtained for **1** and **2** are comparable to those previously determined for the isostructural $Fe^{III}M^{II}$ complexes[33,37,38] (where M^{II} = Zn, Ni, Cu). Interestingly, the increase of ∼0.5 pH units for the M^{III}-bound water molecule when Fe^{III} in **1** is replaced by Ga^{III} to generate complex **2** is in agreement with the first deprotonation of the hexaaqua complexes of Fe^{III} and Ga^{III}, which are pK_{a1} = 2.7 and 3.1, respectively, at 0.1 M.[28−30] However, this decreased acidity in solution is in contrast to the shorter average M^{III}−O distance for M = Ga^{III} versus Fe^{III} in the solid state. Similar results have been obtained for the $Fe^{III}Zn^{II}$ and $Ga^{III}Zn^{II}$ complexes containing the same ligand.[29,33]

Phosphatase-Like Activity. The catalytic activity of complexes **1** and **2** was evaluated in the hydrolysis reaction of the activated substrate 2,4-BDNPP[48] and monitored spectrophotometrically at 400 nm (ε = 12 100 M^{-1} cm^{-1} of the 2,4-DNP^- anion) at 25 °C, as described

Scheme 1. Equilibrium of Chemical Species in CH_3CN/H_2O Solution Proposed for Complexes **1** and **2**

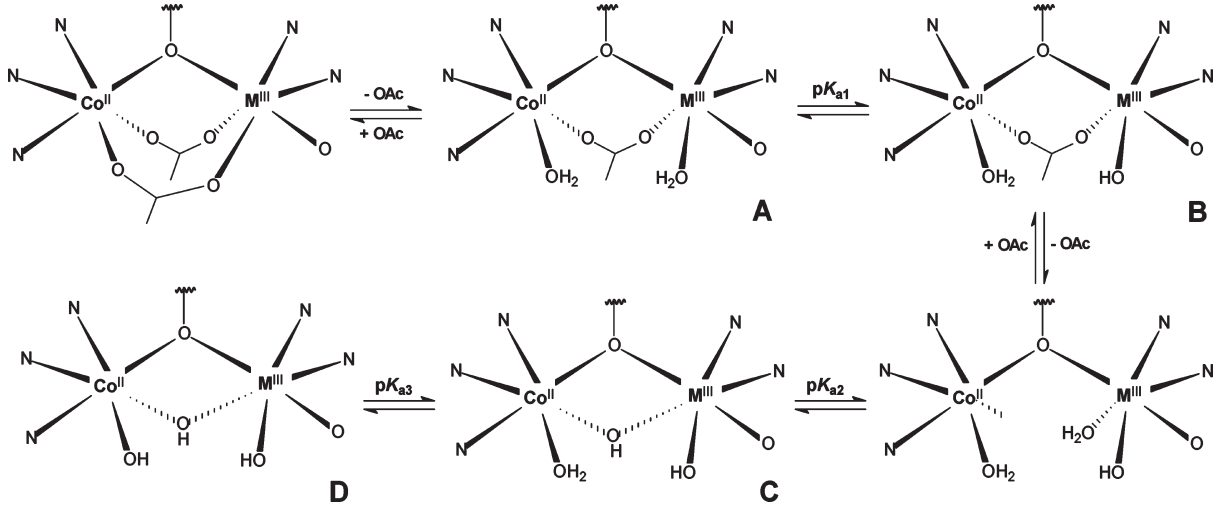

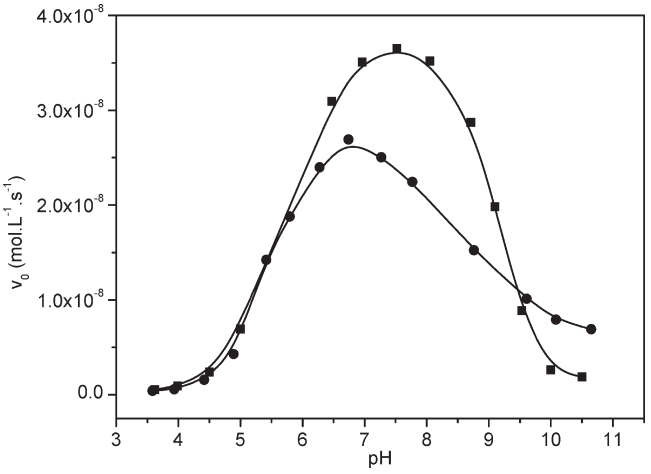

Figure 10. Dependence of the reaction rates (V_0) as a function of pH for **1** (●) and **2** (■) under the following conditions: H_2O/CH_3CN 50% solution, [complex] = 4.0×10^{-5} M, [2,4-BDNPP] = 5.0×10^{-3} M, [buffer] = 8.50×10^{-2} M (MES, HEPES, CHES, CAPS), I = 0.1 M ($LiClO_4$).

elsewhere.[33,37,38] The pH dependence of the catalytic activity between pH 3.5 and 10.0 shows bell-shaped profiles with optima at pH 7.0 and 7.5 for complexes **1** and **2**, respectively (Figure 10). From sigmoidal fits of the curves, two catalytically relevant pK_a values for each complex were obtained (pK_{a1} = 5.2 and pK_{a2} = 8.8 for **1**; pK_{a1} = 5.7 and pK_{a2} = 8.9 for **2**). These pK_a values are in good agreement with the pK_{a1} and pK_{a3} obtained from the potentiometric (Table 4), spectrophotometric titrations (Table 4) and with values for other isostructural $Fe^{III}M^{II}$ complexes, including the $Fe^{III}Ni^{II}$, $Fe^{III}Cu^{II}$, and $Fe^{III}Zn^{II}$ systems.[33,38,39] The combined data indicate that the active species is of the type [(HO)M^{III}-μ-(OH)-$Co^{II}(H_2O)$], as proposed for mammalian[28−30,71] and plant[8] PAPs and for the $Fe^{III}(\mu$-OH)Zn^{II} biomimetic model.[32] Kinetic rates are maximal under conditions where the concentration of active species is predominant, that is, at a pH that lies between the catalytic pK_{a1} and pK_{a2}. At a pH < pK_{a1}, the M^{III}-bound hydroxide ligand (nucleophile) is protonated, thus diminishing the reaction rates. When the pH > pK_{a3}, the Co^{II}-bound water ligand is deprotonated, which reduces the leaving tendency of the hydroxo ligand from the Co^{II} center, thus preventing coordination by the substrate.[32,39]

Saturation kinetics data were obtained at pH 7.00 for complex **1** and at pH 7.50 for complex **2** (Figure 11a), that is, their respective pH optima. The data were fitted to the Michaelis−Menten equation. Linearization of the curves was also carried out using the Lineweaver−Burk method (Figure 11b). The kinetic parameters are listed in Table 5.

The catalytic activity of the $Ga^{III}Co^{II}$ system is approximately 35% higher than that observed for the corresponding $Fe^{III}Co^{II}$ complex at optimal pH, while K_M values are similar for both complexes. Thus, under similar experimental conditions, complexes **1** and **2** catalyze the hydrolysis of the diester 2,4-BDNPP approximately 7500 and 10 000 times faster, respectively, when compared to the uncatalyzed reaction ($k_{uncat} = 1.87 \times 10^{-7}$ s^{-1}).[48] Similar catalytic activity has been determined for the isostructural $Fe^{III}Zn^{II}$ and Ga^{III}-Zn^{II} complexes,[29] but the $Fe^{III}Co^{II}$ and $Ga^{III}Co^{II}$ complexes are slightly more efficient. Importantly, similarly to the biomimetics described here, the Ga^{III} derivatives of bsPAP and Uf are more reactive than their Fe^{III} counterparts,[29,26] suggesting a common catalytic role of the M^{III} center in both the PAPs and the model systems. However, in contrast to PAPs, replacement of the Fe^{III} to Ga^{III} in the model results in a shift of ~0.5 pH units to higher pH for the acid limb of the bell-shaped pH profile, in line with a higher pH optimum for the $Ga^{III}Co^{II}$ system (Figure 10).

In order to elucidate the mode of interaction between the diester substrate 2,4-BDNPP and the dinuclear [(OH)$Fe^{III}(\mu$-OH)$Co^{II}(OH_2)$] catalytic center, we followed the spectral change of the reaction mixture at the pH optimum over a period of 24 h in the presence of excess substrate (Supporting Information, Figure S8). The absorption maximum and the intensity of the phenolate−Fe^{III} charge transfer remains unchanged, which indicates that the substrate does not interact with the Fe^{III}

(70) Lambert, E.; Chabut, B.; Chardon-Noblat, S.; Deronzier, A.; Chottard, G.; Bousseksou, A.; Tuchagues, J. P.; Laugier, J.; Bardet, M.; Latour, J. M. *J. Am. Chem. Soc.* **1997**, *119*, 9424.

(71) Twitchett, M. B.; Schenk, G.; Aquino, M. A. S.; Yiu, D. T. Y.; Lau, T. C.; Sykes, A. G. *Inorg. Chem.* **2002**, *41*, 5787.

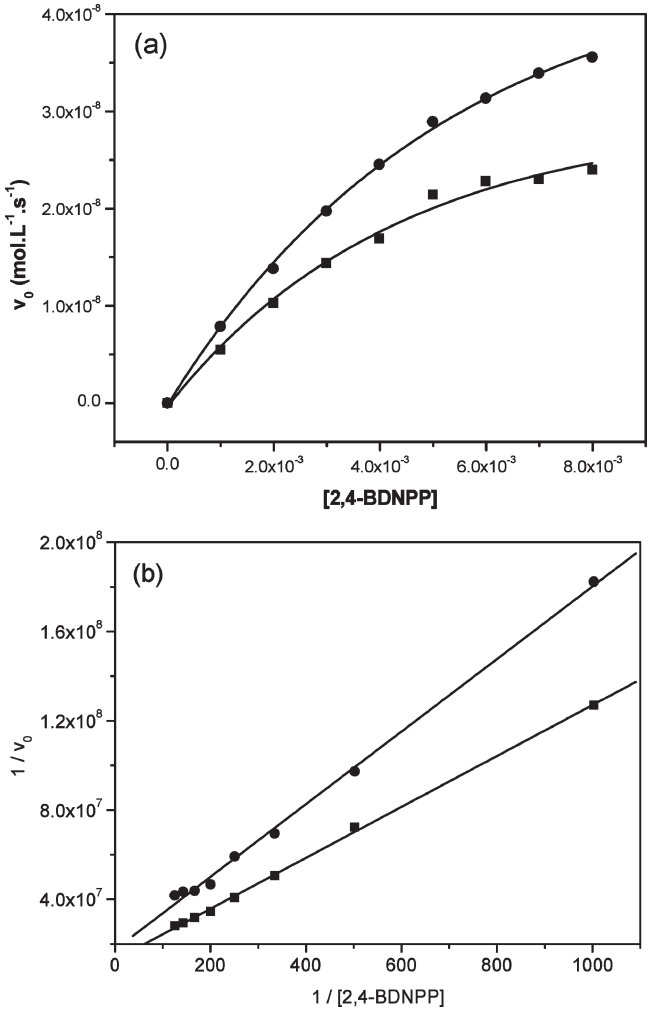

Figure 11. (a) Dependence of the reaction rates on the 2,4-BDNPP concentration for the hydrolytic cleavage catalyzed by **1** (●) and **2** (■), in an acetonitrile/water (50% v/v) mixture solution and (b) the double reciprocal linearization. Conditions: $[complex]_{final} = 4.0 \times 10^{-5}$ M, $[2,4\text{-}BDNPP]_{final} = 1.00 \times 10^{-3}$ to 8.00×10^{-3} mol L^{-1}, $[B]_{final} = 5 \times 10^{-2}$ mol L^{-1}, pH 7.00 (HEPES buffer), at 25 °C.

center, and therefore a monodentate binding of the diester to the Co^{II} can be expected (K_M values are also similar for both complexes, vide infra). On the other hand, the absorption at 400 nm continues to increase due to the formation of stoichiometric amounts of the product 2,4-dinitrophenolate.

We also tested the ability of **1** to hydrolyze the monoester 2,4-DNPP directly with an excess of the substrate, and over a period of 24 h, only the background reaction with the formation of small amounts of 2,4-dinitrophenolate and inorganic phosphate was observed. The coordination of the monoester bridging the two metal ions is proposed on the basis of the bathochromic shift (482 to 500 nm) observed after ligation of 2,4-DNPP to **1**. In addition, the observation that, after 24 h, the hydrolysis of the diester substrate 2,4-BDNPP by **1** and **2** ceases indicates that the monoester formed acts as an inhibitor of the catalytic reaction. This conclusion is in agreement with the observation that, when 2,4-BDNPP is added to the reaction mixture of **1** or **2** with the monoester 2,4-DNPP present, no further hydrolysis of the diester takes place. It is worth nothing that, under similar experimental conditions, the $Fe^{III}(\mu\text{-}OH)Zn^{II}$ catalyst shows around 200 turnovers in 24 h. Thus, in the Co^{II}-containing systems, the product of the first catalytic cycle is likely to remain bound to the biomimetic, preventing the binding of a new substrate molecule. Unfortunately, a direct comparison with the enzymatic system is not possible since data on the kinetic parameters of the hydrolysis of

Table 5. Kinetic Parameters Obtained for the Hydrolytic Cleavage of 2,4-BDNPP Promoted by Complexes **1** and **2**[a]

		kinetic parameters		
complex	k_{cat} (s^{-1})	K_M (mol L^{-1})	K_{assoc} (L mol^{-1})	k_{cat}/k_{uncat}
1	1.42×10^{-3}	9.27×10^{-2}	107.9	7.6×10^3
2	1.87×10^{-3}	8.81×10^{-2}	113.5	1.0×10^4

[a] Conditions: $[complex]_{final} = 4.0 \times 10^{-5}$ M, $[2,4\text{-}BDNPP]_{final} = 6.67 \times 10^{-4}$ to 6.0×10^{-3} M, $[B]_{final} = 5 \times 10^{-2}$ M, pH 7.00 (HEPES buffer), at 25 °C.

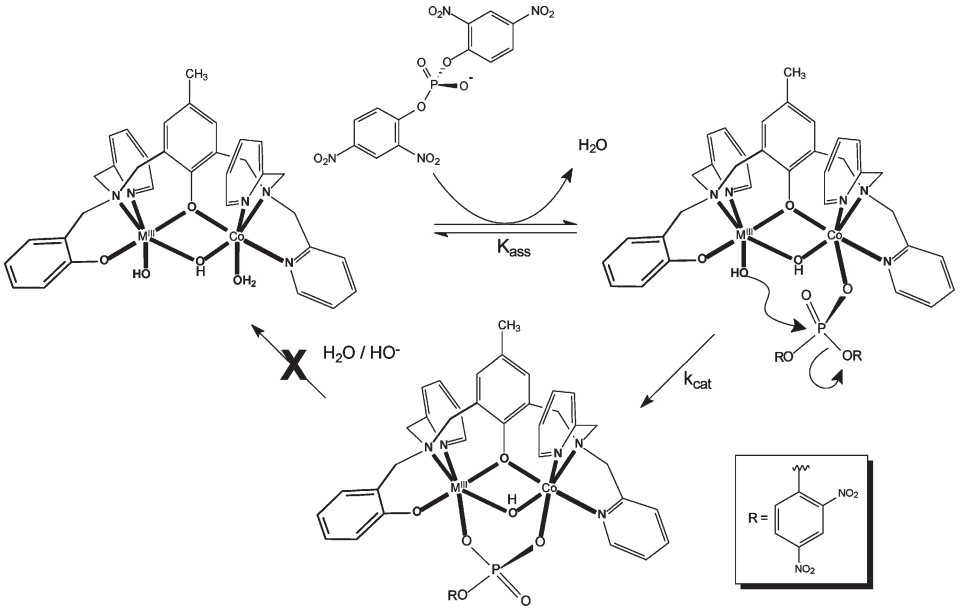

Figure 12. Proposed mechanism for the hydrolysis of 2,4-BDNPP by **1** (M^{III} = Fe) and **2** (M^{III} = Ga).

monoester and diester phosphates by the $Fe^{III}Co^{II}$ enzyme derivative are not available.

Kinetic isotope effect studies for the hydrolytic cleavage of 2,4-BDNPP by **1** and **2** were carried out to probe the catalytic mechanism further. According to Deal et al.,[72] a k_H/k_D ratio between 0.80 and 1.50 for reactions performed in H_2O and D_2O indicates that no proton transfer occurs during the rate-limiting step of the reaction. Therefore, the k_H/k_D values of 1.00 and 0.90 obtained for **1** and **2**, respectively, support the idea of an intramolecular nucleophilic attack by a M^{III}-bound hydroxide in the hydrolysis reaction of the diester 2,4-BDNPP.

Since complexes **1** and **2** are expected to release their μ-acetate bridges under kinetic experimental conditions, competitive inhibition of hydrolysis by acetate ions may occur. However, the presence of 2 equiv of acetate inhibits the catalytic reaction only by ~3% for the hydrolysis reaction, thus confirming the presence of the catalytic initiating species in high concentrations (~75%) in the kinetic studies.

Considering the X-ray structures, potentiometric titration results, and the kinetic behavior of complexes **1** and **2** in the hydrolysis of 2,4-BDNPP, we suggest a mechanism as shown in Figure 12. The dependence of the reaction rates on pH suggests that the initiating nucleophile in the hydrolysis reaction is the terminal M^{III}-coordinated water molecule in complexes **1** and **2**. The kinetic pK_a values are in good agreement with those obtained from potentiometric titration experiments. Small differences in these values are most probably related to the fact that potentiometric pK_a values are associated with the free catalyst, while the kinetic ones obtained from the V_0 versus pH plots (Figure 10) are due to protonation equilibria in the catalyst−substrate complex.[32] The catalytically active species ($[(HO)M^{III}(\mu\text{-}OH)Co^{II}(H_2O)]$) possesses both a Co^{II}-bound water molecule, facilitating the monodentate binding of the substrate molecule, and a M^{III}-coordinated hydroxide nucleophile available for intramolecular attack at neutral pH. The formation of a complex−substrate intermediate is proposed on the basis of the reaction rate versus [substrate] profile (Figure 11), which follows saturation kinetics, in agreement with the Michaelis−Menten model for a catalytic mechanism.

The catalytic reactivity difference between **1** and **2** (Table 5) and the results of the solvent deuterium isotope effect experiments ($k_H/k_D \sim 1.0$) also support the role of the terminal M^{III}−OH acting as a nucleophile in the reaction, as has been proposed previously by Neves et al. for the $[Fe^{III}(\mu\text{-}OH)Zn^{II}]$ system.[32] Thus, the rate-limiting step must involve intramolecular attack of the M^{III}-bound hydroxo group on the phosphorus atom and concomitant release of 2,4-dinitrophenolate. Even under conditions of excess substrate, the kinetics show the release of only 1 equiv of 2,4-dinitrophenolate for **1** and **2**, which suggests the formation of a stable $M^{III}Co^{II}(\mu$-monoester phosphate) complex.

DNA Interaction. In order to set up the experimental conditions for the nuclease-like activity promoted by complexes **1** and **2**, we first evaluated the influence of ionic strength on the DNA cleavage (Figure S9, Supporting Information). The increase in NaCl concentration greatly inhibits the hydrolytic cleavage of pBSK II DNA causing a marked concentration reduction in form II (circular) of the cleaved plasmid, suggesting that opposite charges are involved in the reaction mechanism for both complexes.[73] The effects of the metal complexes' concentration and of pH on the nucleic acid cleavage were also evaluated. Experiments were carried out under identical conditions at pH 6.0, 6.5, and 7.0 with selected metal complex concentrations (0−40 μM) for **1** and **2**, respectively, and the results are shown in Figure 13.

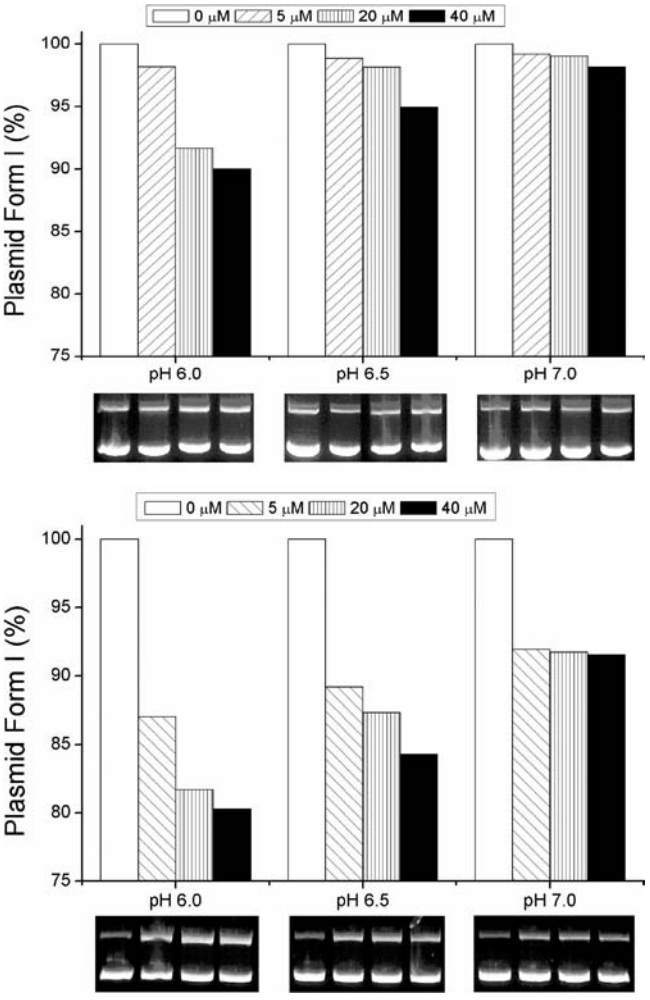

Figure 13. Plasmid DNA cleavage promoted by complexes **1** and **2** (upper and lower, respectively) at pH 6.0, 6.5, and 7.0. Reactions were performed with pBSK II DNA for 16 h at 37 °C in a 25:75% CH_3CN/H_2O PIPES buffer (5 mM) where [**1**] and [**2**] were 0, 5, 20, and 40 μM.

At pH 6.0, cleavage of DNA form I (supercoiled) by **1** is higher, resulting in a proportional increase in form II (circular). According to the potentiometric titration species distribution curves (see the Potentiometric Titration section), under these experimental conditions there is a higher percentage of $[(HO)M^{III}Co^{II}(H_2O)]$. Thus, the $[(HO)M^{III}Co^{II}(H_2O)]$ species is most probably associated with the catalytic activity in the DNA cleavage, as observed in the hydrolysis of the model substrate 2,4-BDNPP. At pH 6.5 and 7.0, the catalytic activities of **1**

(72) Deal, K. A.; Henge, A. C.; Burstyn, J. N. *J. Am. Chem. Soc.* **1996**, *118*, 1713.

(73) Franklyn, S. J. *Curr. Opin. Chem. Biol.* **2001**, *5*, 201.

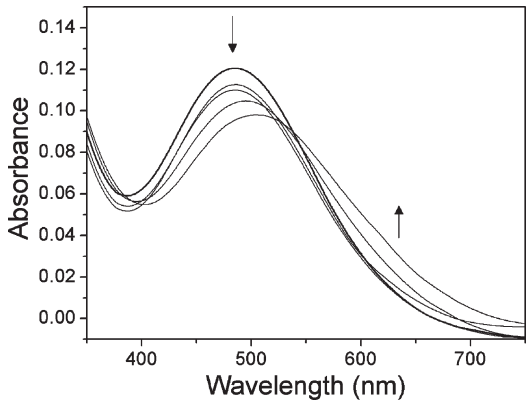

Figure 14. Absorption spectra of complex **1** in the absence (bolded line $R = 0$) and in the presence ($R = 0.05$, 0.1, 0.5, and 1.0) of increasing amounts of CT-DNA. The R values correspond to the ratio [DNA]/[**1**]. Conditions: 25:75% CH_3CN/H_2O PIPES buffer (5 mM) at pH 6.0, [I] = 0.01 M (NaCl), [**1**] = 40 μM, and 25 °C.

and **2** seem to decline, and these results are most probably associated with deprotonation of a water molecule bound to the Co^{II} center. However, it should be noted that pH optima in the cleavage of DNA by **1** and **2** are ~0.5 pH units lower when compared to the values observed in the hydrolysis of 2,4-BDNPP. A plausible interpretation for these distinct results is most probably related to the interaction of the catalyst with the complex structure of DNA.

As observed in the hydrolysis of the model substrate 2,4-BDNPP, the $Ga^{III}Co^{II}$ complex is more active than the corresponding $Fe^{III}Co^{II}$ complex, and DNA cleavage occurs more efficiently at pH 6.0 (Figure 13). These experiments have clearly demonstrated the dependence of DNA cleavage activity by **1** and **2** on pH and complex concentration. Both complexes were able to cleave DNA at a low micromolar concentration under mild pH and temperature conditions, with complex **2** being 2 times more efficient in DNA cleavage than complex **1**. Thus, the results obtained for DNA cleavage by **1** and **2** corroborate the proposed mechanism for the hydrolysis of the model substrate 2,4-BDNPP in which the terminal hydroxo group bound to M^{III} (M^{III} = Fe, Ga) acts as the nucleophile during the catalysis.

Metal complexes are able to interact (covalently or not) with DNA through its nitrogen bases and phosphate groups, establishing strong interactions.[74] In order to address the type of interaction with DNA exhibited by our systems, we performed a spectrophotometric titration of complex **1** in the presence of increasing concentrations of CT-DNA. Titration spectra of **1** in the absence of CT-DNA (bold line, $R = 0$) and in the presence of increasing amounts of DNA ($R = 0.05$, 0.1, 0.5, and 1.0) are shown in Figure 14. Maximum absorption of the free complex was observed at 485 nm. After DNA addition, a clear decrease in molar absorptivity (hypochromism) with a red shift (λ_{max} from 485 to 503 nm) was observed, indicating an interaction with CT-DNA possibly by intercalation. The calculated intrinsic binding constant ($K_b = 1.35 \times 10^5\ M^{-1}$) and red shift suggested a strong binding of **1** with DNA, possibly by intercalation, as compared to other metal complexes described in the literature.[75−78]

Conclusions

We have synthesized and fully characterized two unprecedented dinuclear mixed-valence complexes, $[Fe^{III}Co^{II}(BPBPMP)(\mu\text{-}OAc)_2]ClO_4$ (**1**) and $[Ga^{III}Co^{II}(BPBPMP)(\mu\text{-}OAc)_2]ClO_4$ (**2**), as models for substituted PAPs and nucleases, with the well-known unsymmetrical ligand 2-bis[{(2-pyridylmethyl)-aminomethyl}-6-{(2-hydroxy-benzyl)-(2-pyridyl-methyl)}-aminomethyl]-4-methylphenol. A magnetostructural correlation between the exchange parameter J (cm^{-1}) and the average $Fe^{III}-(\mu\text{-}O_{phenoxo})$ and $M^{II}-(\mu\text{-}O_{phenoxo})$ distances (Å) for **1** and related isostructural $Fe^{III}M^{II}$ complexes revealed that the $[Fe^{III}-(\mu\text{-}O_{phenoxo})-M^{II}]$ structural unit is the major pathway in determining the degree of antiferromagnetic coupling in the series of $[(BPBPMP)Fe^{III}(\mu\text{-}OAc)_2M^{II}]^+$ complexes (M^{II} = Mn, Fe, Co, Ni). HFEPR studies supported the magnetic analysis. Both $[(HO)M^{III}Co^{II}(H_2O)]$ complexes showed significant catalytic activity in the hydrolysis of the phosphate diester 2,4-BDNPP and DNA. On the basis of structural, potentiometric and spectrophotometric titration and kinetic data, a catalytic mechanism which involves intramolecular nucleophilic attack of a terminal M^{III}-coordinated hydroxo group on the phosphorus atom of the diester phosphate bound to the Co^{II} center with a concomitant release of 2,4-dinitrophenolate was proposed. Finally, it was also demonstrated that complexes **1** and **2** are specific catalysts for phosphodiester bonds since no reaction with the activated monoester 2,4-dinitrophenolate was observed.

Acknowledgment. The authors are grateful for grants that helped to support this research: CNPq, FAPESC and INCT-Catálise (Brazil), BMBF/IB (Germany), and the NHMFL (IHRP grant #5062 J.K. and J.T.), which is funded by NSF (Cooperative Agreement DMR 0654118), the State of Florida, and the DOE. The 25-T magnet at NHMFL was funded by the W. M. Keck Foundation. We thank Prof. Brian M. Hoffman (Northwestern University) for use of the 35 GHz EPR spectrometer, which is funded by the NIH (grant HL13531).

Supporting Information Available: Figures S1−S9, showing a 35 GHz EPR spectrum of **2**; MCD data for **1** and **2**; UV−vis spectra for **1** and **2**; cyclic voltammograms for **1** and **2**; species distribution of **1** and **2**; spectrophotometric titration of **1** phosphodiester and DNA cleavage data. This material is available free of charge via the Internet at http://pubs.acs.org.

(74) (a) Chao, H.; Mei, W.-J.; Huang, Q.-W.; Ji, L.-N. *J. Inorg. Biochem.* **2002**, *92*, 165. (b) Otero, L.; Smircich, P.; Vieites, M.; Ciganda, M.; Severino, P. C.; Terenzi, H.; Cerecetto, H.; Gambino, D.; Garat, B. *J. Inorg. Biochem.* **2007**, *101*, 74. (c) Tamilarasan, R.; McMillin, D. R. *Inorg. Chem.* **1990**, *29*, 2798. (d) Rey, N. A.; Neves, A.; Bortoluzzi, A. J.; Pich, K. T.; Terenzi, H. *Inorg. Chem.* **2007**, *46*, 348.

(75) Chan, H.-L.; Liu, H.-Q.; Tzeng, B.-C.; You, Y.-S.; Peng, S.-M.; Yang, M.; Che, C.-M. *Inorg. Chem.* **2002**, *41*, 3161.

(76) Zhang, S.-S.; Niu, S.-Y.; Qu, B.; Jie, G.-F.; Xu, H.; Ding, C.-F. *J. Inorg. Biochem.* **2005**, *99*, 2340.

(77) Mahadevan, S.; Palaniandavar, M. *Inorg. Chem.* **1998**, *37*, 693.

(78) Reddy, P. R.; Rao, K. S.; Satyanarayana, B. *Tetrahedron Lett.* **2006**, *47*, 7311.